

# Confidence levels for tsunami-inundation limits in northern Oregon inferred from a 10,000-year history of great earthquakes at the Cascadia subduction zone

George R. Priest · Chris Goldfinger · Kelin Wang · Robert C. Witter · Yinglong Zhang · António M. Baptista

Received: 3 March 2009 / Accepted: 25 August 2009  
© Springer Science+Business Media B.V. 2009

**Abstract** To explore the local tsunami hazard from the Cascadia subduction zone we (1) evaluate geologically reasonable variability of the earthquake rupture process, (2) specify 25 deterministic earthquake sources, and (3) use resulting vertical coseismic deformations for simulation of tsunami inundation at Cannon Beach, Oregon. Maximum

A brief summary of this paper was presented at the December 2008 San Francisco meeting of the American Geophysical Union. A technical report releasing digital data and technical details of the study (on CD) is available in Priest et al. (2009).

G. R. Priest (✉) · R. C. Witter  
Newport Coastal Field Office, Oregon Department of Geology and Mineral Industries,  
Newport, OR, USA  
e-mail: george.priest@dogami.state.or.us  
URL: <http://www.oregon.gov/DOGAMI/FIELDOFFICES/fieldoffice.shtml>

R. C. Witter  
e-mail: rob.witter@dogami.state.us.or  
URL: <http://www.oregongeology.com/sub/FIELDOFFICES/profile-witter.htm>

C. Goldfinger  
Oregon State University, Corvallis, OR, USA  
e-mail: gold@oce.orst.edu  
URL: <http://www.coas.oregonstate.edu/index.cfm?fuseaction=content.search&searchtype=people&detail=1&id=540>

K. Wang  
Geological Survey of Canada, Pacific Geoscience Centre, Sidney, BC, Canada  
e-mail: kwang@nrcan-rncan.gc.ca  
URL: [http://cgc.nrcan.gc.ca/dir/index\\_e.php?id=8400](http://cgc.nrcan.gc.ca/dir/index_e.php?id=8400)

Y. Zhang · A. M. Baptista  
OGI School of Science and Engineering, Oregon Health & Science University, Portland, OR, USA  
e-mail: yinglong@ccalmr.ogi.edu  
URL: [http://www.ogi.edu/people/dsp\\_person.cfm?person\\_id=411D67F7-2A56-D16D-58DF61EA167BA0E4](http://www.ogi.edu/people/dsp_person.cfm?person_id=411D67F7-2A56-D16D-58DF61EA167BA0E4)

A. M. Baptista  
e-mail: baptista@ebs.ogi.edu  
URL: <http://www.stccmop.org/node/41>

---

runup was 9–30 m (NAVD88) from earthquakes with slip of  $\sim 8\text{--}38$  m and  $M_w \sim 8.3\text{--}9.4$ . Minimum subduction zone slip consistent with three tsunami deposits was 14–15 m. By assigning variable weights to the source scenarios using a logic tree, we derived percentile inundation lines that express the confidence level (percentage) that a Cascadia tsunami will *not* exceed the line. Ninety-nine percent of Cascadia tsunami variation is covered by runup  $\leq 30$  m and 90%  $\leq 16$  m with a “preferred” (highest weight) value of  $\sim 10$  m. A hypothetical maximum-considered distant tsunami had runup of  $\sim 11$  m, while the historical maximum was  $\sim 6.5$  m.

**Keywords** Tsunami · Cascadia · Oregon · Paleoseismic · Deterministic · Earthquake

### Abbreviations

DOGAMI Oregon Department of Geology and Mineral Industries  
TPSW Tsunami Pilot Study Working Group  
CSZ Cascadia subduction zone  
MHHW Mean higher high water

## 1 Introduction

Tsunamis from  $\sim M_w$  8 to 9 earthquakes on the Cascadia subduction zone pose a significant threat to the Pacific Northwest Coast of the US and Canada (e.g., Atwater et al. 1995, 2005; Dragert and Hyndman 1995; Satake et al. 2003; Nelson et al. 2006). Similar magnitude earthquakes from far-field sources have had only modest impact to this coast (Lander et al. 1993). For this reason, and because computations of near-field tsunami impact are highly sensitive to details of source deformations such as asperities (Titov et al. 2001), we focused primarily on development of a practical method for characterization of the tsunami hazard posed by a local Cascadia subduction zone earthquake. We achieve this objective through comprehensive earthquake source characterization of the north-central Cascadia subduction zone combined with numerical simulations of tsunami flooding at Cannon Beach, Oregon (Fig. 1). We chose Cannon Beach for its relatively small size, variety of topography, rich record of Cascadia tsunami deposits, and detailed historical observations of tsunami inundation from the 1964 tsunami generated by the  $M_w$  9.2 Prince William Sound Earthquake in the Gulf of Alaska. Technical details of the investigation and digital data files are available in Priest et al. (2009).

## 2 Approach

We estimate the range of plausible Cascadia subduction zone earthquake sources in the vicinity of Cannon Beach, Oregon (Fig. 1) using data on the geometry and tectonic behavior of the subduction zone (Goldfinger et al. 1992, 1997, 2007; Mitchell et al. 1994; Hyndman and Wang 1995; McCrory et al. 2004; McCaffrey et al. 2007) and evolving inferences on size and frequency of earthquakes over the last 10,000 years derived from the offshore turbidite record (modified after Goldfinger et al. 2008 and summarized in Goldfinger et al. 2009). We assume that fault slip must roughly equal plate convergence

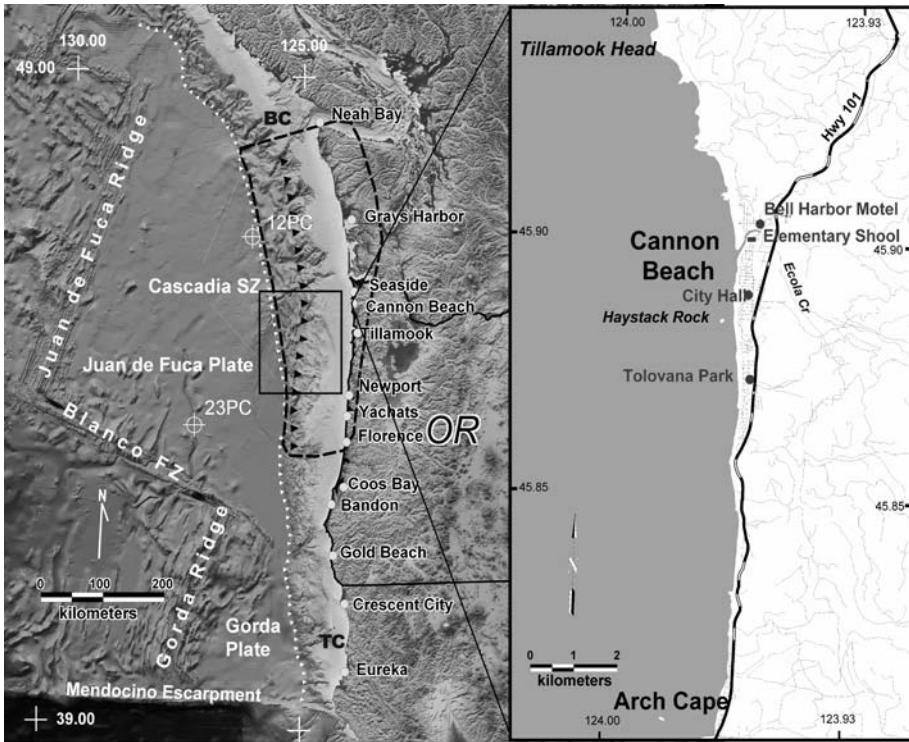


**Fig. 1** Location of the Cannon Beach study area (*right panel*) relative to major offshore tectonic plates and plate boundaries (*left panel*). *Dashed bold line in left panel* is the portion of the Cascadia subduction zone simulated for coseismic deformation. *Small white triangles* mark the Cascadia subduction zone megathrust; *large black triangles* mark a splay fault used for tsunami simulations; *solid black rectangle* is the map area of Fig. 6; *white circles with crosses* are core sites for turbidite mass data of Table 1. FZ = fracture zone; SZ = subduction zone; BC = Barkley Canyon; TC = Trinidad Canyon. These two submarine canyons mark the northern and southern limits of available turbidite data

(coupling ratio = 1.0), and that variations in time intervals between offshore turbidites are representative of variations in coseismic slip. We then specify four representative slips and test the effect on tsunamis of slip partitioned into forearc basins, forearc banks, a regional locked zone, a splay fault, and with variable seaward skew. After weighting each tsunami scenario through a logic tree, we depict the resulting inundations on maps in terms of percent confidence that a local Cascadia tsunami will reach no further inland than each boundary line.

We examine the hazard from distant tsunamis only for two extreme cases: the largest historical event, the 1964 Alaska tsunami, and a hypothetical maximum-considered event from the Gulf of Alaska taken from the Tsunami Pilot Study Working Group (TPSW 2006) investigation of Seaside, Oregon (Fig. 1).

Comparison of results to historical and paleoseismic observations provided a ground truth check. Simulated Cascadia coseismic deformation and tsunami inundation was checked for a match to paleoseismic estimates of recurrence, paleosubsidence, and minimum inundation. Standard benchmark tests and comparison of observed to simulated inundation of the 1964 tsunami provided an estimate of accuracy for the hydrodynamic model, SELFE.

---

### 3 Relation to previous work

Unlike most previous studies of the Cascadia tsunami hazard (e.g., Hebenstreit and Murty 1989; Ng et al. 1990; Preuss and Hebenstreit 1998; Priest 1995; Priest et al. 1997, 2007; TPSW 2006; Walsh et al. 2000; Whitmore 1993), this investigation evaluates far more Cascadia earthquake sources and uses a logic tree to systematically explore geologically reasonable variations in source parameters. Previous tsunami hazard assessments by the State of Oregon (e.g., Priest et al. 1997, 2007) have for the most part simulated three Cascadia earthquake sources, two utilizing uniform slip and one maximum event using a Gaussian uplift patterned after uplift at the largest asperity inferred from seismic data on the 1964 Prince William Sound earthquake (Priest et al. 1997). Unlike the TPSW (2006) Cascadia sources, earthquake sources for this investigation are multi-deterministic rather than probabilistic, and we assume that coseismic slip decreases up dip on the Cascadia megathrust owing to velocity-strengthening behavior (Wang and He 2008). We further assume that the wide Pliocene–Pleistocene accretionary wedge in northern Cascadia has velocity-strengthening behavior that prevents the extreme seaward skew of slip assumed by the TPSW (2006).

Most recent investigations of tsunami hazard to the Pacific Northwest coast focused on the Cascadia hazard as does this investigation; an exception is the TPSW (2006) study that explored 14 distant sources. The TPSW (2006) demonstrated that all but the most extreme distant sources pose little threat to the nearby town of Seaside, Oregon. This finding provided a quantitative basis for our decision to explore only a maximum teletsunami of the TPSW investigation (their Gulf of Alaska Source 3) and the largest historical teletsunami, the 1964 tsunami from the Prince William Sound Earthquake.

### 4 Methods

#### 4.1 Geological constraints on Cascadia earthquake source parameters

##### 4.1.1 Paleoseismic recurrence for estimation of fault slip

Following the method of Rikitake (1999), we use earthquake recurrence as a proxy for fault slip. The degree of aseismic slip is unknown, so we assume conservatively (higher tsunami hazard) that coupling ratio is 1.0. When we consider all offshore paleoseismic data, the along-strike correlations of turbidites described by Goldfinger et al. (2003a, b, 2008, 2009), and relevant high quality onshore data, including those of Witter (2008) and Atwater et al. (2004), we infer that in the Holocene, the Cascadia subduction zone effectively had four rupture modes: 19 long ruptures with variable southern limits (some of which are imposed by data availability); two distinct ruptures comprising the southern 60% of the margin, and 18 smaller southern margin ruptures during the Holocene that have variable northern and southern limits (Goldfinger et al. 2008, 2009). Turbidite observations are only available from Barkley Canyon on the north to Trinidad Canyon on the south, a north–south distance of ~800 km (Fig. 1). There is some uncertainty as to the northern limits of some of these events. One of the large southern ruptures (T10f) and two of the smaller ones (T5b and T9a) may reach the latitude of Cannon Beach. We assume that at least one of these (T5b) reaches Cannon Beach and therefore use 20 events here to determine local interseismic intervals and calculate the local earthquake recurrence of ~500 years (Table 1). Erring on the side of caution, we calculate slip for a maximum-considered Cascadia event from the

**Table 1** Paleosubsidence (degree of coastal wetland submergence) events in southwest Washington and the Columbia River from Atwater et al. (2004) compared to turbidite data from Goldfinger et al. (2009 from prepublication data released June 23, 2009)

SW WA land sub. event	SW WA land sub. event age range >95% CI (years)	SW WA land sub. from/to	Turb. event	Norm. turb. mass Core 12 PC (WA)	Norm. turb. mass Core 23PC (OR)	Turb. mean age (years)	Turb. age error +2σ (years)	Turb. age error -2σ (years)	Turb. follow time (years)
Y	250	Forest/Mud	T1	175	155	269 [250]	96	100	>309
-	-	-	T2	115	60	446	85	89	196
W	760-1,165	Marsh/Mud	T3	155	135	784	103	112	338
U	1,230-1,265	Marsh/Mud	T4	110	135	1,198	122	113	414
S	1,549-1,610	Forest/Mud	T5	115	235	1,567	176	167	369
-	-	-	T5b	105	100	2,020	163	159	453
N	2,400-2,625	Marsh/Mud	T6	295	225	2,550	137	147	530 (983)
L	2,850-2,930	Forest/Mud	T7	340	315	3,034	134	163	484
J	3,310-3,395	Forest/Mud	T8	390	170	3,514	168	176	480
-	-	-	T9	290	140	4,158	165	184	644
-	-	-	T10	150	75	4,744	173	189	543
-	-	-	T11	460	625	5,593	148	135	882
-	-	-	T12	40	45	6,289	151	138	707
-	-	-	T13	260	110	7,142	124	118	853
-	-	-	T14	105	105	7,624	139	139	482
-	-	-	T15	100	60	8,187	138	143	563
-	-	-	T16	450	1,110	8,889	197	187	702
-	-	-	T17	90	195	9,142	259	292	253
-	-	-	T17a	60	55	9,203	177	193	61
-	-	-	T18	95	195	9,819	184	232	616

The most accurate age of the last event, T1, is 250 years (AD1700) based on tsunami simulations of Satake et al. (1996); this age is shown in brackets. Follow times are listed because there is a moderate correlation of turbidite mass (and thus potentially earthquake size) to follow times, according to Goldfinger et al. (2009). The follow time for T2 assumes that T1 was deposited in AD 1700. The follow time shown in parentheses for T6 is the time without T5b. Turbidite T5b was not deposited along the entire Cascadia margin like the other turbidites (see discussion in text). Land Sub. Event = coastal wetland submergence event inferred from paleoseismic data; CI = confidence interval; years = years before AD 1950; SW WA. = southwest Washington; OR = Oregon; Turb. = turbidite; Norm. = normalized; Mud = mudflat; dash = no data

maximum recurrence of the 19 full-margin events (i.e., excluding event T5b) plus the  $2\sigma$  error in age data. This maximum interval is between events T5 and T6 and equals  $\sim 1,300$  years, once  $2\sigma$  error is added.

The rupture lengths inferred by Goldfinger et al. (2009) are constrained by the distance between submarine canyons where turbidites are deposited. In each canyon, completely unconnected tributary channels have the same number of Holocene turbidites as the main channel, thus each turbidite is constrained to be synchronous to within several minutes (Adams 1990; Goldfinger et al. 2003a, 2008, 2009). Only Cascadia earthquakes can produce this degree of synchronicity (Adams 1990; Goldfinger et al. 2009). Ages of coastal wetland submergence events in southwestern Washington and the Columbia River from Atwater et al. (2004) are similar to turbidites, but there is no record in southwestern Washington of a submergence event or tsunami deposit correlating with the second youngest turbidite, T2. Also, T2 is one of the smallest margin-wide turbidites, and we suspect that it was not recorded at many land sites due to minimal coastal subsidence, but at present, we do not know exactly why there is no record of T2 in southwestern Washington.

We selected recurrences of  $\sim 300$ , 525, 750, and 1,300 years of plate convergence to represent the family of interevent intervals. Figure 2 compares the frequency of turbidite interevent times relative to these scenario recurrence intervals. The largest mean recurrence interval is 983 years, ranging from 660 to 1,287 years at the  $2\sigma$  error level (Table 1; Fig. 2). The 660–1,287 years range represents the interval between T5 and T6, which was difficult to constrain tightly (see Goldfinger et al. 2009 for detailed discussion). This interval excludes turbidite T5b. The presence or absence of T5b at the latitude of Cannon Beach strongly influences the time-based maximum slip, reducing the largest mean T5–T6 interval from 983 to 530 years ( $2\sigma$  range of 220–826 years) (Table 1). However, this

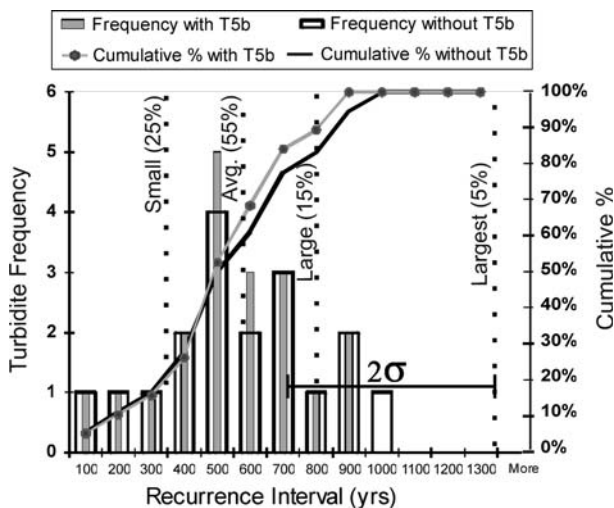


**Fig. 2** Frequency of inter-turbidite time intervals (100-years bins) for the last 10,000 years compared to the four recurrence scenarios (see dotted lines) used for basal branches of the logic tree. Logic tree weights assigned to each scenario are in parentheses. Illustrated are frequencies for intervals between all 20 turbidites (solid bars) and for intervals without turbidite T5b (open bars) relative to cumulative percent of intervals (lines). The  $2\sigma$  error on the maximum recurrence interval for recurrence data without turbidite T5b is shown encompassing the “Largest” recurrence scenario. Turbidite T5b extends only as far north as  $44^{\circ}\text{N}$ , and may extend as far north as Juan de Fuca Canyon, which includes the latitude of Cannon Beach; the other 19 turbidites occur throughout the Cascadia margin

illustrates the uncertainties in the time-based model, as T5b was not large enough to be recorded as a tsunami or coastal subsidence, and therefore probably played a minor role in strain accumulation during the T5–T6 interval, yet it has a disproportionate effect on our time-based maximum slip model. A similarly long interval, the time elapsed between T11 and T10, was even more difficult to evaluate because of the difficulty in dating T11. The T11 event, one of the largest of the Cascadia turbidites, had ubiquitous basal erosion, a problem common to the largest events, increasing the errors involved in dating and interpretation of the age. The final average ages and intervals in Goldfinger et al. (2009) reflect decisions made about which ages for each of these events represent the best quality results as opposed to the averaged full range of  $^{14}\text{C}$  data for each event. In this paper, we take the conservative approach and use for our “Largest” event a recurrence of  $\sim 1,300$  years, fitting the outer envelope of the  $2\sigma$  root mean square error of the largest recurrence. We view using the wider  $2\sigma$  error range as erring on the side of caution, consistent with standard engineering practice and uncertainties in the age data noted by Goldfinger et al. (2009). This recurrence translates to a maximum slip of  $\sim 38$  m at the latitude of Cannon Beach, similar to maximum slip inferred for the 1960 Chile earthquake (Barrientos and Ward 1990).

#### 4.1.2 Up-dip limit of interplate coupling

We assumed that the most seaward segment of the megathrust will release little coseismic energy due to velocity-strengthening behavior during rupture of the weakly coupled portion of the outermost megathrust (Wang and Hu 2006; Wang and He 2008). We therefore tapered slip to zero at the deformation front. Priest et al. (2009) summarize geologic evidence of weak interplate coupling in the outermost part of the Cascadia megathrust; key observations include the following:

1. A widespread landward vergent province in Cascadia coinciding with widely spaced, open folds, suggesting poor interplate coupling (Goldfinger et al. 1992, 1996, 1997; Mandal et al. 1997), and presence of a mud volcano seaward of the Washington deformation front (Goldfinger 1994).
2. A well-defined boundary between landward and seaward vergent structures.
3. Change in strike, wedge taper change, and bathymetric break in slope coinciding with the vergence change.
4. Variable signature of lower plate strike-slip faults that only breach the upper plate in regions of strong coupling inferred from geologic structure of the upper plate (Goldfinger et al. 1992, 1996, 1997).

These observations of the Cascadia subduction zone are consistent with the fault slip model of the Sumatra–Andaman Islands earthquake of December 26, 2004 (Chlieh et al. 2007). Chlieh et al. (2007) also infer decrease in slip up dip from the forearc high into the outer accretionary wedge (Fig. 3).

#### 4.1.3 Down-dip limit of interplate coupling

The down-dip limit of interplate coupling establishes how far landward the megathrust rupture and resulting seafloor deformation will reach. In this report, we use published thermal (Hyndman and Wang 1995; Flück et al. 1997) and GPS based models (McCaffrey et al. 2007) and a geologic proxy for down-dip coupling to constrain the down-dip limit of Cascadia megathrust ruptures. The geologic proxy is a structural transition from

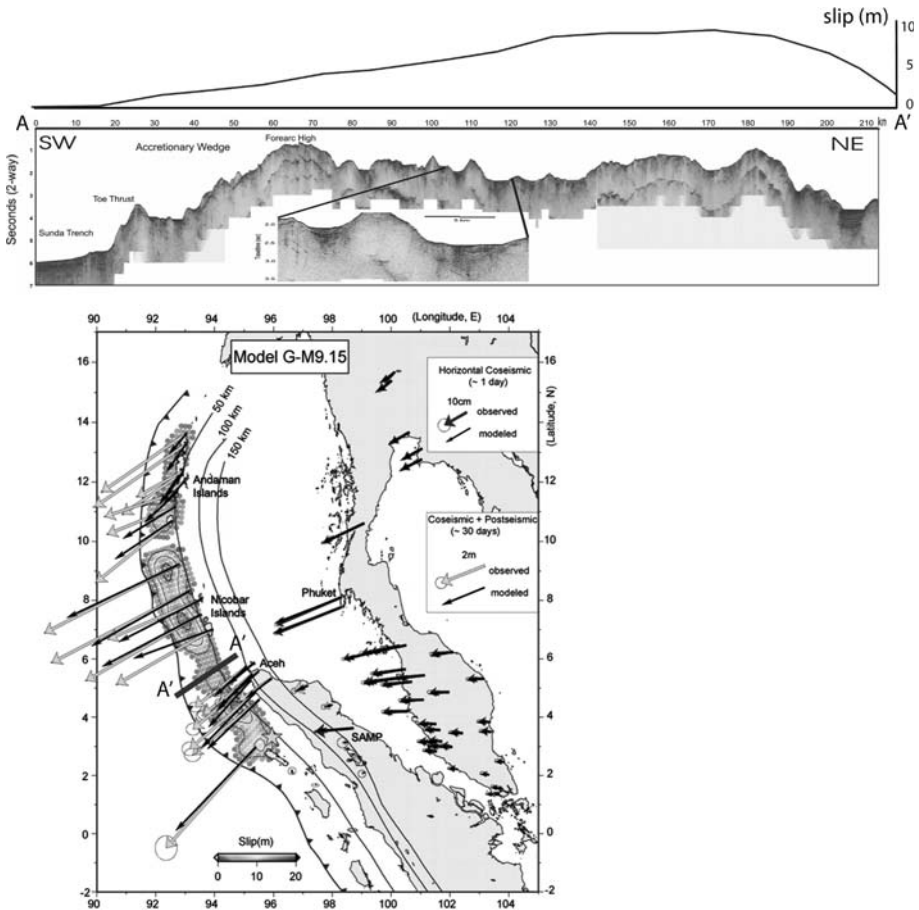


**Fig. 3** Sumatra forearc shown by single channel profile (A–A′) SEATOS line 1 (taken from Fisher et al. 2007). Forearc basin at right, forearc high in center, and subduction thrust (labeled Toe Thrust) and the abyssal plain (Sunda Trench) at left. Lower panel shows preferred slip distribution from Chlieh et al. (2007) for the Sumatra–Andaman Islands earthquake of December 26, 2004, in map view based on GPS data. Profile of the Chlieh et al. (2007) slip distribution along cross section A–A′ is shown above the SCS (single channel seismic) profile. Map location of the subduction zone megathrust on the map is the black line with triangles pointing down the fault dip; dark gray lines to the east are depth contours on the megathrust. Contours in shades of gray on lower map are inferred coseismic slip; arrows show direction and magnitude of observed and modeled coseismic and post-seismic slip, as indicated in the map legend

contraction to extension on the Cascadia margin observable in offshore seismic reflection data, focal mechanisms and borehole breakouts. We interpret this transition as likely representing long-term average interplate coupling and note that it is compatible with thermal and GPS models that cover different time ranges. We tapered slip down dip to points broadly consistent with this geologic limit or “stress boundary” while still achieving a best fit to available paleoseismic estimates of coastal subsidence during the AD 1700 earthquake from the Leonard et al. (2004) compilation. The 1700 earthquake in general appears to be a “typical” event based on the turbidite record, and thus may represent an average rupture scenario. We also did fault model trials to obtain a best match to the Leonard et al. (2004) data.

While there is no certainty that the mapped pattern of contractional and extensional structures actually reflects plate coupling, observations of the 2004 and 2005 earthquakes in Sumatra suggest that this may be the case. Models of the Sumatra slip distribution such as those derived from GPS (Chlieh et al. 2007; Fig. 3) and seismologically (Ammon et al. 2005) suggest that the down-dip extent of seismogenic slip roughly corresponds to the transition from the arcward part of the forearc high to the lightly deformed forearc basin (Goldfinger and McNeill 2006). A review of less well-recorded great earthquakes such as Kamchatka (1952), Alaska (1964), and Chile (1960) yields ambiguous interpretations, slightly favoring a similar interpretation (Goldfinger et al. 2007). The 1960 Chile earthquake may be an exception, because there is some evidence that it ruptured beneath the forearc basin (Barrientos and Ward 1990).

In Cascadia, we map a transition similar to that of Sumatra based on the following observations:

1. The Cascadia forearc high is probably an area of contraction and thus high compressional stress, since the high consists of seaward vergent thrust faults in an imbricate stack (Fig. 4). These faults also form the western limb of the forearc basin and are observed as flexural slip faults developed within stratigraphic horizons of the forearc basin stratigraphy (Fig. 4).
2. Forearc basins are probably areas of extension and low compressional stress, since, as shown in the Fig. 4, contractional deformation of the basin is limited to the western edge, gives way to relatively undeformed stratigraphy in the basin center and landward limb.
3. The change from contractional to extensional structures across the seaward limbs of the forearc basins forms a regular pattern (Fig. 5). We used the youngest structures available, though only approximate temporal control is available from a few test wells (McNeill et al. 2000). Note that evidence of extension of the Washington shelf shown in Fig. 5 as a cluster of white dots corresponds to shallow listric normal faulting (McNeill et al. 1997) and is probably not relevant to coupling on the megathrust.
4. Earthquake focal mechanisms (Global Centroid Moment Tensor Database 2007; Trehu et al. (2008), and various sources) and borehole breakout data (Werner et al. 1991) indicate a change in compressional axis from convergence-parallel (northeast) to arc-parallel (north-south) at approximately the boundary between contractional to extensional forearc structures (Fig. 5).

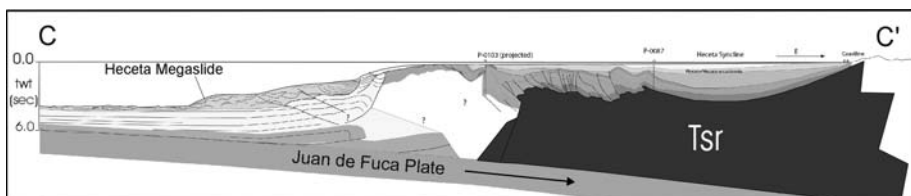


**Fig. 4** Cross section across Heceta Bank, Oregon from Chevron line HOG 15 and Western Geco line WO-18. This typical forearc section shows the compressional nature of the forearc basin (contrast with section of Wells et al. 2003, along the same profile). Flexural slip faulting controls the basin western margin, the eastern margin is undeformed or extensional. Boundary between extension and compression is mapped for numerous similar profiles in Fig. 5. See Fig. 5 for location of this cross section. Unit Tsr is Siletz River Volcanics of the Siletzia terrane considered to be a hard rock backstop in contact with sedimentary rocks of the accretionary prism (bedded units) to the west. Twf is two-way travel time

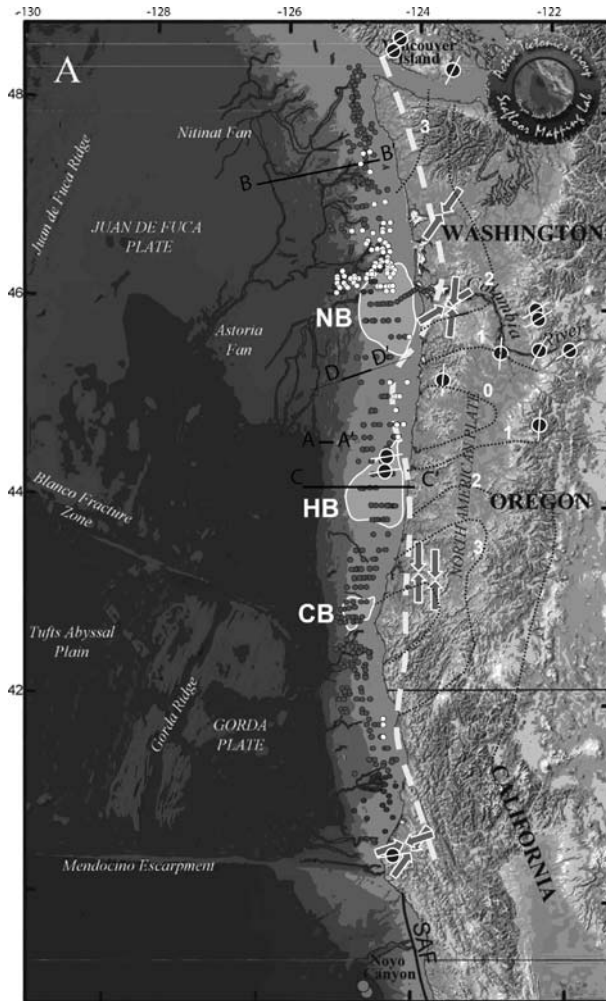


**Fig. 5** Compilation of geologic stress indicators along the central Cascadia margin. *Dark gray dots* show compressive structure locations, *white dots* show extensional structures mapped along multichannel reflection profiles. *Gray arrows with white outlines* show P-axes from borehole breakouts, *Black circles with white axes* show P-axes from focal mechanisms from the Global Centroid Moment Tensor Database. *Black dotted contours* show geodetic uplift contours of Mitchell et al. (1994). Three structural uplifts known as Nehalem Bank (NB), Heceta Bank (HB), and Coquille Bank (CB) shown as *light gray polygons with white outlines*. *Bold dashed line* shows mean stress transition (“stress line”) from compressive to extensional indicators. See text and Priest et al. (2009) for data source references

5. The stress boundary in Fig. 5 is compatible with other down-dip estimates of coupling based on thermal models (Hyndman and Wang 1995; Flück et al. 1997), leveling data (Mitchell et al. 1994; Schmidt et al. 2007; Burgette et al. 2009) and GPS data (McCaffrey et al. 2007).

Each of these indicators cannot strictly be compared to the others as they represent different physical properties and different time scales. Nevertheless, the combined data are quite consistent and seem to represent a coherent transition from convergence-related

compression to arc-parallel compression that is well known in the Cascadia forearc (Wang and He 1999).

#### 4.1.4 Interplate coupling at forearc basins and banks

The stress boundary shown in Fig. 5 (supported by leveling and tide gauge data) suggests that broad regions of the upper plate where the stress line swings landward coincide with major structural uplifts. The central Oregon region where the stress line swings seaward coincides with a deep structural and gravity low (McNeill et al. 2000). In Oregon, two of the structural uplifts correspond to free-air gravity highs and are known as Coquille, and Heceta Banks, while the third Nehalem Bank, is a gravity low (Fig. 5; see gravity map of Wells et al. 2003). We suggest that the map pattern of inferred higher coupling corresponding to the submarine banks may indicate regions of high slip during subduction earthquakes because the GPS and leveling data suggest greater present interseismic elastic strain that must be released in earthquakes, while the stress line indicates greater long-term strain. This pattern is clearly apparent in Sumatra, where the 2007, 2005, and 2004 rupture patches were for the most part centered over analogous structural highs, tapering landward into the undeformed forearc basin, and seaward into the outer wedge (Chlieh et al. 2007; Konca et al. 2008).

Wells et al. (2003) suggest an alternative model. They argue on the basis of global comparisons of earthquake slip models with gravity data, that seismic moment is concentrated beneath forearc basins. While this model appears to work well for several well-known cases such as Nankai and Chile, it failed to predict the Sumatra 2004 distribution of slip or slip distributions of the other largest known earthquakes such as Kamchatka (1952) and Alaska (1964). The basin model proposed by Wells et al. (2003) is also incompatible with the structural data outlined earlier as it requires the forearc basins to be fully extensional features. A related model by Song and Simons (2003) suggests that slip is concentrated in trench-parallel gravity lows, a proposal similar to but distinct from that of Wells et al. (2003). Though these models are commonly linked, the Song and Simons model subtracts an average gravity profile, and identifies lows from the resulting data, something not done in the Wells et al. model. The Song and Simons model also fails to predict slip distributions in Sumatra.

At present, it is not possible to determine which of these models, if any, is operative in Cascadia. We produced simulations of coseismic deformation for both basin and bank slip patch models but give less weight in our decision tree to the basin model.

#### 4.1.5 Splay fault

Common along subduction margins with thick incoming sedimentary sections is a major splay fault that separates the active accretionary wedge from an older accretionary complex. These splay faults may have also generated tsunamis or contributed to tsunami generation during subduction zone earthquakes (e.g., Plafker 1972; Park et al. 2002). Along the central Cascadia margin ( $\sim 45^\circ\text{N}$  to  $47^\circ\text{N}$ ), this fault is well expressed and marks the boundary between the low tapering lower slope wedge and steeper tapering upper slope and shelf accretionary complex (Figs. 6, 7). On a northern Oregon proprietary profile and on depth-migrated Sonne lines 103 and 108 (Adam et al. 2004), the approximate fault dip is  $\sim 30^\circ$ . Some profile crossings such as that of Fig. 7 suggest recent seafloor offset, and thus recent fault activity.

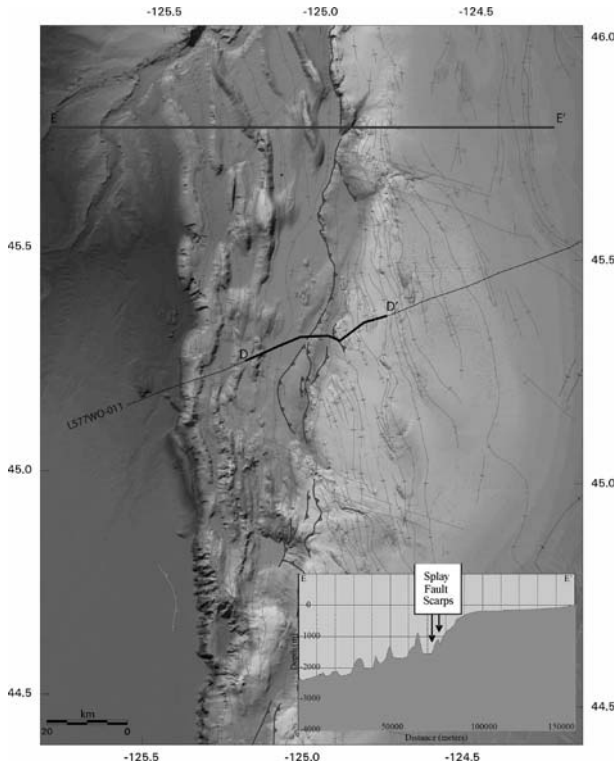


**Fig. 6** Shaded bathymetry of the Oregon margin, with structural map overlay (Goldfinger 1994). The lower slope (*medium gray* with rough topography) is characterized by (1) landward vergence; (2) low surface taper (profile E–E’); (3) wide fold spacing and is dominated by margin parallel folds. Older accretionary complex (*lighter gray* to the east) is dominated by convergence-normal fold trends landward vergence, and steep mid-slope defining a steeper wedge taper. The two provinces are separated by a seaward vergent splay fault (*bold gray lines with triangles* pointing down the thrust fault dip) and abrupt break in surface slope. Mapped traces of the splay fault scarps are shown in this figure; generalized location of the model fault used for the tsunami source models is depicted on Fig. 1. Splay fault is imaged by USGS reflection profile L-5-WO77-12, shown in Fig. 7. Bathymetric profile (profile E–E’) with vertical exaggeration of 1:16.7 shows low surface wedge taper, and steep upper slope separated by the splay fault scarps. See Fig. 1 for location of this map

Given the evidence for recent movement, the clear domain boundary between older and younger accretionary complexes, and the structural indications of a significant difference in deformation style, we infer that the Cascadia splay fault is a significant structure capable of diverting slip from the décollement to the surface as has been suggested for the Nankai margin (Cummins et al. 2001). We use a generalized fault deformation model of this fault (Fig. 1) to explore the effect on tsunami runup and inundation.

#### 4.2 Cascadia fault rupture simulation

All simulations of surface deformation from Cascadia fault rupture scenarios employ the point source solution from Okada’s (1985) dislocation model and emulate coseismic deformation between 43.9°N near Florence, Oregon to ~47.9°N at Neah Bay, Washington (Fig. 1). Compared to the importance of and large uncertainties in the slip distribution,

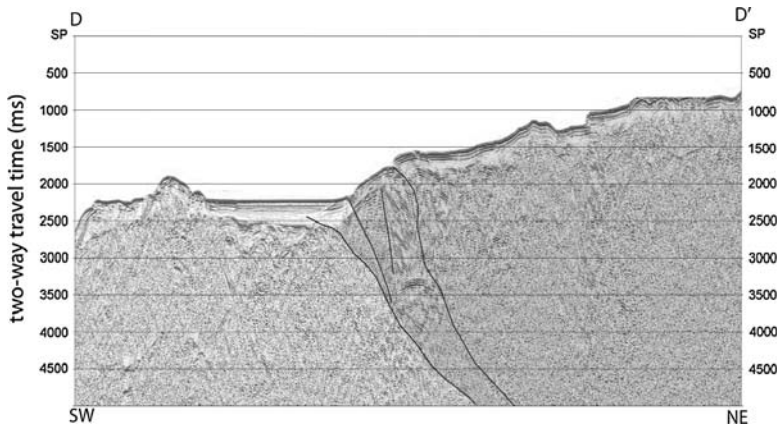


**Fig. 7** Unmigrated USGS reflection profile L-5-WO77-12 across the mid-slope off north-central Oregon. Splay fault separating young wedge (west) from older accretionary complex (east) is imaged as a zone with two major traces and active upward branches (Mann and Snavelly 1984). Young basin fill is deformed by the upward branching fault, and upper trace breaks the seafloor at this location. Lower slope is characterized by a more open fold style, and landward vergence indicative of less interplate coupling than the upper slope seaward vergent fold and thrust belt. See Fig. 6 for location and further depiction of vergence changes. SW is southwest; NE is northeast

other factors such as material heterogeneity, inelastic behavior, dynamic deformation, and horizontal seafloor motion are of secondary concern. Therefore, the model of a uniform elastic half-space with a Poisson's ratio of 0.25 is employed in this work. Attention is paid mainly to the most critical issue of how to assign coseismic slip along the Cascadia megathrust.

Slip direction of the coseismic rupture is assumed to be exactly opposite of plate convergence. The plate convergence direction and rate are calculated from Euler vectors as explained in Wang et al. (2003) and account for convergence between the Juan de Fuca Plate and the North American Plate, including reduction of convergence by forearc rotation (McCaffrey et al. 2000, 2007).

Megathrust geometry is modified from that of McCrory et al. (2004). In the McCrory et al. (2004) model, because depth is measured from sea level, the depth of the megathrust is over 5 km at the deformation front, where the actual water depth to the seafloor is 2–3 km. To let the upper surface of the elastic half-space approximately represent the seafloor, the most up-dip part of the megathrust is “raised” to 2–3 km depth by resetting the 5-km slab surface contour of McCrory et al. (2004) (located seaward of the deformation front) to 2 km. This “raised” structure contour line and other contour lines of McCrory et al. (2004) at 5 km intervals are used to construct the megathrust geometry using GMT program “Surface.”

All of the fault ruptures are simulated utilizing the slip function of Wang and He (2008) modified from the fb76 slip distribution of Freund and Barnett (1976). Fundamental to the Wang and He (2008) approach is recognition that the seismogenic zone of subduction faults has an up-dip limit, seaward of which the fault exhibits velocity-strengthening behavior. This view is supported by observed and inferred coseismic seafloor deformation of great subduction zone earthquakes, particularly that associated with the 2004, 2005, and 2007 Sumatra events (Fig. 3). Therefore, all rupture simulations incorporate coseismic slip tapering to zero at the deformation front. In a real megathrust earthquake, the slip varies

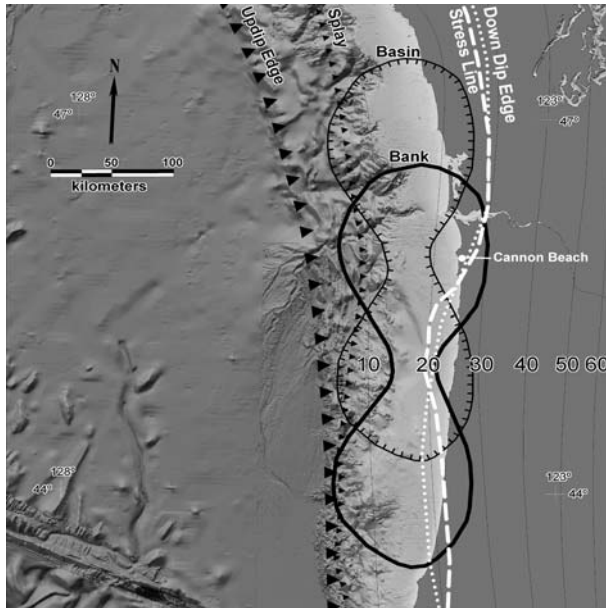


**Fig. 8** Structural boundaries relevant to this work. *Thin lines* are depth contours at 10 km intervals to the Cascadia megathrust. *Large triangles* are the surface trace of the megathrust (up-dip edge of regional slip patches); *small triangles* are the model splay fault; basin slip patch is the *hachured line*; bank slip patch is the *bold black line*; the “stress line” where crustal contraction changes eastward to crustal extension is the *dashed white line*; modeled down-dip extent of regional slip patches is indicated by the *dotted white line*

tremendously along strike giving rise to the concept of asperities. Because we cannot predict where the maximum slip will occur along strike, we use a “regional slip patch” model to simulate an average uniform scenario. Local slip patches are assumed to be at either basins or banks and are simulated by quadratically scaling maximum slip with down-dip and up-dip patch width. Each assumed slip distribution on the megathrust for splay fault models is simply truncated at the surface trace of the splay fault. Figure 8 shows boundaries of the simulated splay fault, local basin and bank slip patches, and the regional slip patch. The down-dip boundary of the regional slip patch was constrained by both the previously discussed “stress boundary” and by a best fit to available coseismic subsidence data of Leonard et al. (2004). We found that use of seaward skew ( $q = 0.3$ ) for regional slip patches produced a somewhat poorer fit than symmetrical slip ( $q = 0.5$ ) to onshore paleoseismic estimates of coseismic subsidence, as did varying the rupture width by 20 km (Fig. 9).

### 4.3 Logic tree evaluation of Cascadia earthquake source parameters

The parametric analysis of tsunami sources was guided by a logic tree with branches arranged from most to least important controls on vertical coseismic deformation for Cascadia earthquakes (Fig. 10). The four earthquake source parameters chosen, from most to least important, are

1. Earthquake size (coseismic slip)
2. Presence or absence of a splay fault

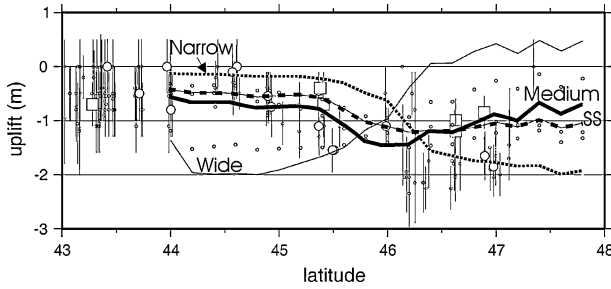


**Fig. 9** Coastal subsidence predicted by buried rupture, regional slip patch models utilizing 500 years of slip release and comparison with AD 1700 coseismic subsidence data. The approximate mean recurrence of Cascadia earthquakes is 500 years. *Square* and *large circles* indicate best quality and better quality data as explained in Leonard et al. (2004). Models utilize a symmetric slip distribution but vary rupture width by  $\pm 20$  km from the best fit width to geologic data; *bold line* = preferred medium-width rupture patch), *dotted line* = 20 km narrower, and *thin line* = 20 km wider. To test for sensitivity of tsunami simulations to seaward-skewed (SS) slip ( $q = 0.3$ ), one model was constructed utilizing a medium patch width (*dashed line*)

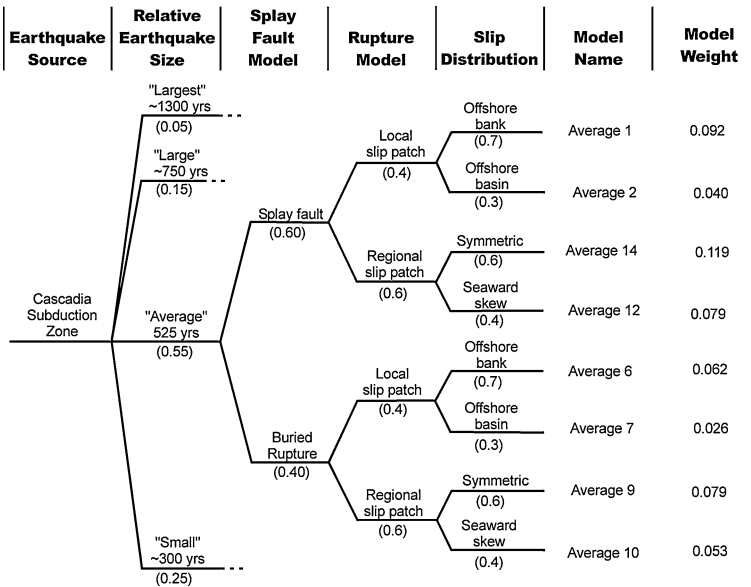


**Fig. 10** Logic tree for selection and relative weighting of Cascadia tsunami sources. See the text and Tables 2 and 3 for detailed summaries of the weighting factors for all branches

3. Fault rupture extent (regional rupture or local basin/bank rupture), and
4. Slip distribution (symmetrical within banks or basins and symmetrical or seaward skewed within regional slip patches).

Weighting factors were assigned by the scientific team (authors of this paper) to each branch of the logic tree based on consensus and observational geologic data at Cascadia and other potentially analogous subduction zones. Therefore, weights represent the relative confidence or preference of the scientific team. The weights do not reflect the temporal

probability of the next tsunami. Table 2 shows a summary of the weighting factors and reasons for the weights. Table 3 summarizes all Cascadia scenarios and their logic tree weights. Figure 11 illustrates map views of the eight coseismic deformation scenarios for slip equaling 525 years of plate convergence (our “Average” scenarios in the logic tree).

In order to save computational time and avoid simulating many small events with similar, small inundations, we utilized only one of the eight “small” earthquake sources for slip equaling  $\sim 300$  years of plate convergence, Small 9; hence, we used only 25 of the 32 Cascadia scenarios. Small 9 had the highest logic tree weight for the “small” branch and consisted of a regional slip patch with symmetric slip and no splay fault (buried rupture on the megathrust). For relative hazard computations, we assigned all eight of the “small” logic tree weights to this one scenario, increasing its weight from 0.072 to 0.25 (Table 3).

**Table 2** Explanation of logic tree weights

Coseismic slip	Each scenario is assigned a weight according to the number of earthquakes of a particular size that are recorded in the $\sim 10,000$ -year record of 20 Cascadia turbidites. For data available in 2007, a weight of 0.05 applies to the “largest” slip, because one of the 20 events had an interseismic interval of $\sim 1,300$ years; 3 of 20 events were “large” events assigned a weight of 0.15; 11 out of 20 were moderate in size, or “average” events assigned a weight of 0.55; and 5 of 20 were considered “small” events and weighted at 0.25.
Slip partitioned to a splay fault	Weighting factors assigned in this branch reflect greater likelihood that larger slip events will trigger coseismic slip on a splay fault. For the “largest” and “large” scenarios, the ratio of weights assigned to splay fault versus buried rupture events is 0.8:0.2. For “average” scenarios, the ratio is 0.6:0.4. For “small” events, the ratio is the opposite of that used for the largest scenarios, or 0.2:0.8
Rupture model	The regional slip patch model was assigned a higher weight (0.6) than local ruptures in forearc basins and banks (0.4), because (1) the trench-parallel length of local slip patches is highly uncertain, whereas the regional slip patch substantially includes all local slip patches; (2) turbidite data are consistent with long ruptures as the primary rupture type experienced in the northern Cascadia margin (Goldfinger et al. 2008); and (3) landward extent of the regional slip patch is constrained by the “stress line” of Fig. 5 and to consistency with paleoseismic estimates of coseismic subsidence (Fig. 9)
Slip distribution: basin versus bank slip patches	Higher weight (0.7) to slip patches concentrating slip at forearc banks versus forearc basins (0.3), because mapped structures within the banks are contractional, indicating greater strain accumulation possibly linked to strong coupling on the locked zone beneath the banks. Structures under the centers and landward limbs of basins are extensional indicative of lesser strain accumulation from the megathrust locked zone (see text for discussion)
Slip distribution for regional slip patches: symmetric versus seaward skewed	The symmetric slip distribution (weight of 0.6) was judged more likely than the seaward-skewed slip (weight of 0.4), because the skewed distribution results in poorer fit to coastal paleosubsidence data of Leonard et al. (2004) for the 1700 AD Cascadia event (Fig. 9)

**Table 3** Earthquake source parameters and weighting factors used in logic tree. Slip listed in the table is maximum slip for each slip distribution and is estimated for the latitude of Cannon Beach

Rupture scenario	Slip (m)	$M_w$	Splay fault/ buried rupture	Rupture model	Slip distribution	Total weight factor
Largest 1 (0.05)	~ 38	~ 8.8	Splay (0.8)	Local (0.4)	Offshore bank (0.7)	0.011
Largest 2 (0.05)	~ 38	~ 8.8	Splay (0.8)	Local (0.4)	Offshore basin (0.3)	0.005
Largest 14 (0.05)	~ 38	~ 9.2	Splay (0.8)	Regional (0.6)	Symmetric (0.6)	0.014
Largest 12 (0.05)	~ 38	~ 9.2	Splay (0.8)	Regional (0.6)	Seaward skew (0.4)	0.010
Largest 6 (0.05)	~ 38	8.8	Buried rupture (0.2)	Local (0.4)	Offshore bank (0.7)	0.003
Largest 7 (0.05)	~ 38	8.8	Buried rupture (0.2)	Local (0.4)	Offshore basin (0.3)	0.001
Largest 9 (0.05)	~ 38	9.3	Buried rupture (0.2)	Regional (0.6)	Symmetric (0.6)	0.004
Largest 10 (0.05)	~ 38	9.3	Buried rupture (0.2)	Regional (0.6)	Seaward skew (0.4)	0.002
Large 1 (0.15)	~ 22	~ 8.6	Splay (0.8)	Local (0.4)	Offshore bank (0.7)	0.034
Large 2 (0.15)	~ 22	~ 8.6	Splay (0.8)	Local (0.4)	Offshore basin (0.3)	0.014
Large 14 (0.15)	~ 22	~ 9.1	Splay (0.8)	Regional (0.6)	Symmetric (0.6)	0.043
Large 12 (0.15)	~ 22	~ 9.1	Splay (0.8)	Regional (0.6)	Seaward skew (0.4)	0.029
Large 6 (0.15)	~ 22	8.6	Buried rupture (0.2)	Local (0.4)	Offshore bank (0.7)	0.008
Large 7 (0.15)	~ 22	8.6	Buried rupture (0.2)	Local (0.4)	Offshore basin (0.3)	0.004
Large 9 (0.15)	~ 22	9.1	Buried rupture (0.2)	Regional (0.6)	Symmetric (0.6)	0.011
Large 10 (0.15)	~ 22	9.1	Buried rupture (0.2)	Regional (0.6)	Seaward skew (0.4)	0.007
Average 1 (0.55)	~ 15	~ 8.5	Splay (0.6)	Local (0.4)	Offshore bank (0.7)	0.092
Average 2 (0.55)	~ 15	~ 8.5	Splay (0.6)	Local (0.4)	Offshore basin (0.3)	0.040
Average 14 (0.55)	~ 15	~ 9.0	Splay (0.6)	Regional (0.6)	Symmetric (0.6)	0.119
Average 12 (0.55)	~ 15	~ 9.0	Splay (0.6)	Regional (0.6)	Seaward skew (0.4)	0.079
Average 6 (0.55)	~ 15	8.5	Buried rupture (0.4)	Local (0.4)	Offshore bank (0.7)	0.062
Average 7 (0.55)	~ 15	8.5	Buried rupture (0.4)	Local (0.4)	Offshore basin (0.3)	0.026
Average 9 (0.55)	~ 15	9.0	Buried rupture (0.4)	Regional (0.6)	Symmetric (0.6)	0.079
Average 10 (0.55)	~ 15	9.0	Buried rupture (0.4)	Regional (0.6)	Seaward skew (0.4)	0.053
Small 1 (0.25)	~ 8	~ 8.3	Splay (0.2)	Local (0.4)	Offshore bank (0.7)	0.000 [0.014] <sup>a</sup>
Small 2 (0.25)	~ 8	~ 8.3	Splay (0.2)	Local (0.4)	Offshore basin (0.3)	0.000 [0.006] <sup>a</sup>
Small 14 (0.25)	~ 8	~ 8.9	Splay (0.2)	Regional (0.6)	Symmetric (0.6)	0.000 [0.018] <sup>a</sup>
Small 12 (0.25)	~ 8	~ 8.9	Splay (0.2)	Regional (0.6)	Seaward skew (0.4)	0.000 [0.012] <sup>a</sup>
Small 6 (0.25)	~ 8	8.3	Buried rupture (0.8)	Local (0.4)	Offshore bank (0.7)	0.000 [0.056] <sup>a</sup>
Small 7 (0.25)	~ 8	8.3	Buried rupture (0.8)	Local (0.4)	Offshore basin (0.3)	0.000 [0.024] <sup>a</sup>

**Table 3** continued

Rupture scenario	Slip (m)	$M_w$	Splay fault/ buried rupture	Rupture model	Slip distribution	Total weight factor
Small 9 (0.25)	~ 8	8.9	Buried rupture (0.8)	Regional (0.6)	Symmetric (0.6)	0.250 [0.072] <sup>a</sup>
Small 10 (0.25)	~ 8	8.9	Buried rupture (0.8)	Regional (0.6)	Seaward skew (0.4)	0.000 [0.048] <sup>a</sup>

Slips at other latitudes vary from these values according to estimates of plate convergence rate from the Euler pole of Wang et al. (2003). Convergence rate used to estimate slip for this table is 28.9 mm/year, the appropriate value at the latitude of Cannon Beach.  $M_w$  values are calculated assuming rigidity of 40 GPa, the appropriate slip distribution for each source scenario, and maximum slip determined from plate convergence assuming complete coupling. Areal extents assumed in  $M_w$  calculations for basin and bank slip patch sources are given in Fig. 11; areal extent for regional slip patch sources are assumed to be the entire margin. Symbol ~ means  $M_w$  estimated rather than calculated based on similarity of slip amount between splay fault and buried rupture sources and narrower east–west extent of splay fault slip patches relative to buried ruptures

*Note:* numbers in parentheses are weighting factors assigned to individual branch parameters. In each row, the product of the four weights is equal to the total weighting factor used for the earthquake source scenario

<sup>a</sup> Weighting factors in brackets were assigned to “small” scenarios in the initial logic tree (32 branches). The final logic tree (25 branches) assigned a single weight equal to the sum of all small scenario weights to “Small 9”

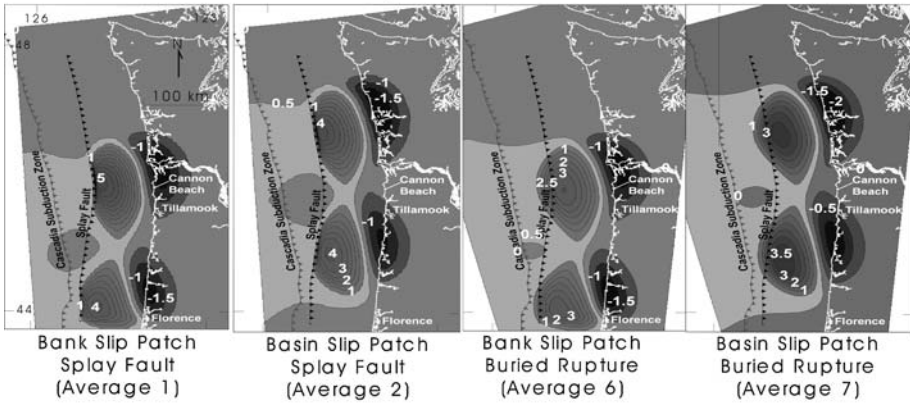
#### 4.4 Distant tsunami sources

We investigated two distant tsunami scenarios in order to simulate the largest historical event and a hypothetical maximum-considered event; both tsunamis are triggered by  $M_w$  of ~9.2 earthquakes in the Gulf of Alaska (Figs. 12, 13). The vertical deformation inferred by Johnson et al. (1996) provided the initial condition for simulation of the largest historical event, the 1964 Prince William Sound earthquake (Fig. 12). The maximum-considered event is the hypothetical Source 3 of the TPSW (2006) that in their investigation caused the largest distant tsunami at Seaside, Oregon, 9 km north of Cannon Beach (Fig. 1). This source has four segments with 15, 20, 25, and 30 m of slip (see TPSW’s Table 6, p. 41) and maximum uplift over twice as high as that inferred for the 1964 earthquake (Figs. 12, 13). This large uplift is in a relatively narrow “spike” near the surface trace of the fault and is caused by a singularity in the Okada (1985) uniform slip model (Vasily Titov 2008, personal communication). According to Titov (2008, personal communication) the “spike” has little effect on the resulting tsunami relative to the broader area of 3–5 m uplift to the northwest. TPSW (2006) concluded that better directivity to the northern Oregon coast causes the larger size of this tsunami relative to the 1964 event.

#### 4.5 Hydrodynamic tsunami modeling

Vertical components of deformation from the 25 Cascadia and the two Alaska earthquake sources were used as instantaneous static deformations for tsunami simulations. The finite element model SELFE (Zhang and Baptista 2008) simulated propagation and inundation with an unstructured numerical grid utilizing post-earthquake topography. Grid spacing for simulation of local Cascadia sources varied from 200 m at the source to 2.2 m in parts of Cannon Beach with detailed topographic data (Figs. 14, 15). Deep ocean propagation of the two distant tsunamis utilized grid spacing on the order of 11 km. Each Cascadia simulation was run for at least 2 h of “tsunami time.” Some simulations were run longer (up to 8 h of “tsunami time”) in order to check the importance of inundation from later

Local Slip Patches



Regional Slip Patches

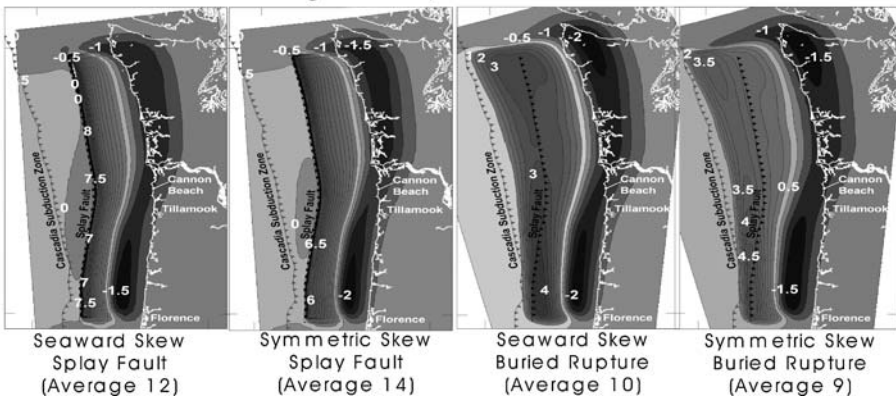


**Fig. 11** Vertical coseismic deformation patterns for release of 525 years of convergence on the Cascadia subduction zone. *White numbers* are deformation in meters, positive = uplift; negative = subsidence; contours are at 0.5 m. Bank slip patch models place slip under submarine banks; basin models under submarine basins; slip is quadratically scaled to the width of the basin or bank. Regional slip patch models place slip west of the “stress line” in Figs. 5 and 8 in either a symmetric ( $q = 0.5$ ) or seaward-skewed ( $q = 0.3$ ) distribution. Splay fault scenarios cut off the slip distribution at the splay fault, amplifying uplift from increase of fault dip to  $30^\circ$

refracted waves or to accommodate propagation from the two distant tsunami sources in Alaska. An 8-h simulation of a Cascadia source revealed that wave height decreased significantly after 2 h, so later arriving waves were smaller and did not “stack” in lowlands; hence, 2 h of “tsunami time” was simulated for most Cascadia sources.

4.6 Tides

All simulations in this investigation were run at 2.711 m above geodetic mean sea level NAVD 1988 based on mean higher high water (MHHW) at the Astoria, Oregon tide gauge. Neglecting non-linear effects, the TPSW (2006) did a probabilistic analysis of tides for Seaside, Oregon and concluded that the effect of tides for a 500-year Cascadia tsunami decreased open coastal run-up by 0.7 m from their assumption of tide at mean high water.

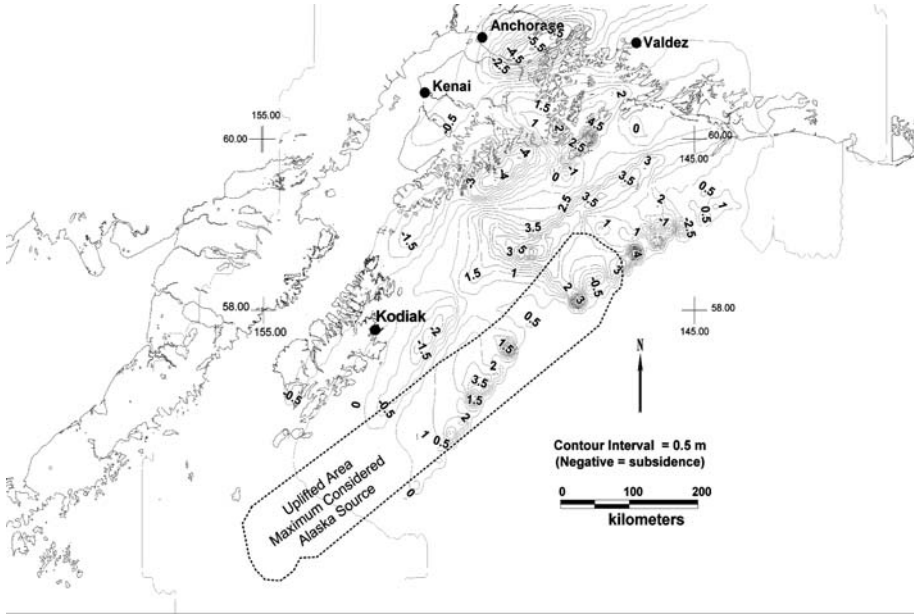


**Fig. 12** Coseismic deformation from the 1964 Prince William Sound earthquake from Johnson et al. (1996); Negative numbers = meters coseismic subsidence; positive numbers = meters coseismic uplift. Shown for comparison is the area of uplift from the theoretical maximum-considered distant tsunami source of Fig. 13

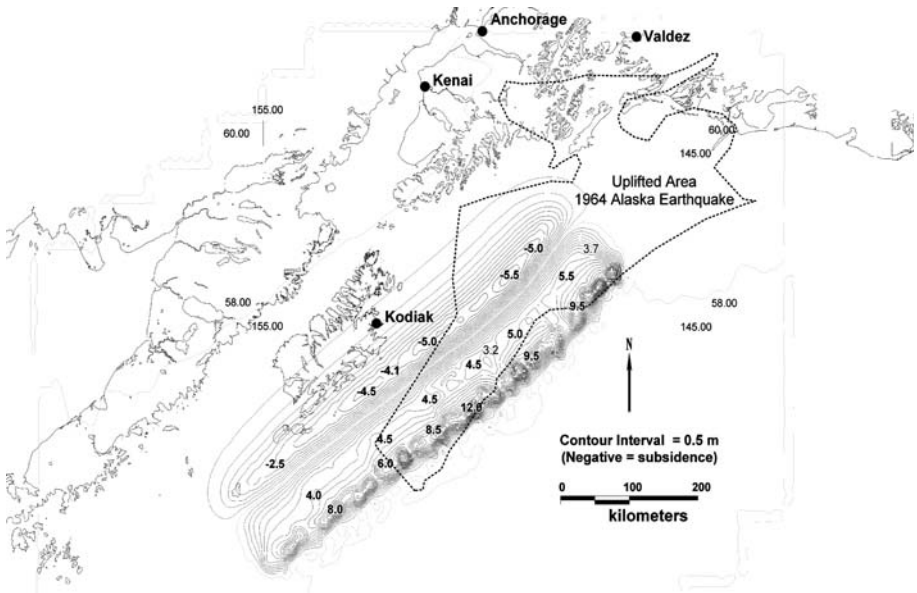


**Fig. 13** Maximum-considered distant tsunami source from the TPSW (2006) analysis for Seaside, Oregon; Negative numbers = meters coseismic subsidence; positive numbers = meters coseismic uplift. Shown for comparison is the area of uplift from the 1964  $M_w$  9.2 earthquake (Fig. 12)

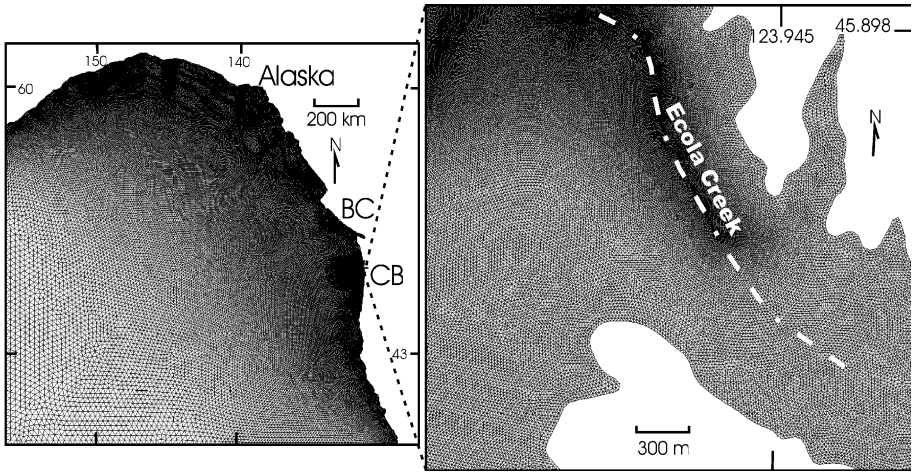
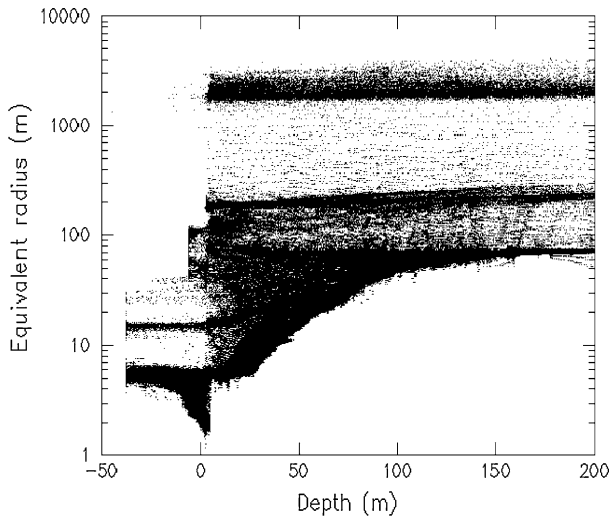


**Fig. 14** Unstructured computational grid used in tsunami simulations. The *left panel* shows the full grid and the *right* is a zoom-in near the Ecola Creek. BC = British Columbia; CB = Cannon Beach

**Fig. 15** Grid resolution expressed as the equivalent radius of each numerical grid element plotted against bathymetric depth [negative depths are above mean higher high (MHHW)]. Graph demonstrates that resolution changes gradually from tens of kilometers in the deep ocean to a few meters on land



Our assumption of MHHW for the Cascadia tsunami simulations is therefore conservative. This tide is  $\sim 0.3\text{-m}$  higher than the tide during initial arrival of the 1964 tsunami from Prince William Sound (Priest et al. 2009).

#### 4.7 Comparison of simulated tsunamis to observations

Distribution of three prehistorical (paleotsunami) deposits and observations of historical tsunami inundation from the 1964 tsunami from Witter (2008) served as ground truth checks of the tsunami modeling approach. Inland reach of paleotsunami deposits marks the minimum inundation of Cascadia tsunamis. Ages of the three deposits from Witter (2008)

---

allowed comparison of relative size of earthquakes to relative inundation. Match of simulated inundation, run-up, and flow depths to observations of the tsunami from the 1964 Prince William Sound earthquake tested accuracy of the hydrodynamic model and inputs. Tsunami simulations used as inputs digital elevation models of the modern topography for the 1964 simulation and prehistorical landscapes for paleotsunami simulations.

#### 4.8 Reconstructing the prehistorical landscape

A 1,000-year B.P. (before AD 1950) landscape (digital elevation model) was constructed by removal of artificial fills from the modern landscape and inferring the paleolandscape from analysis of coastal erosion data, and cores. One thousand years corresponds approximately with the age of the Cascadia tsunami deposit that reaches furthest inland of the three deposits mapped in the Ecola Creek valley by Witter (2008). The landscapes were reconstructed by:

1. Increasing relief on the Ecola Creek valley by  $\sim 1$  m, based on the observation that sea level  $\sim 1,000$  years ago was  $\sim 1$  m lower (Witter 2008) and that sedimentation in coastal Oregon estuaries keeps up with rising sea level.
2. Moving the shoreline at sedimentary rock bluffs and attached sand spits 70 m seaward to account for 1,000 years of erosion. The erosion rate was estimated from historical rate data of Allan and Priest (2001) and of Priest and Allan (2004); see details of the calculation in Priest et al. (2009).
3. Constructing two landscapes, one with foredune height the same as present, and one with no barrier dune fronting the estuary.

#### 4.9 Comparison of simulated coseismic deformation to observations

Another means of testing validity of the simulations is to compare simulated coseismic subsidence for Cascadia scenarios to subsidence estimated from paleosubsidence data. We used data compiled by Leonard et al. (2004) and Nelson et al. (2008) for the AD 1700  $\sim M_w$  9 Cascadia earthquake (Satake et al. 2003), an “average” event in terms of turbidite mass and thickness (proxies for earthquake size) compared to other turbidites in the 10,000-year record (Table 1; Goldfinger et al. 2009; Priest et al. 2009).

## 5 Results

### 5.1 Cascadia earthquake sources

Modeled coseismic uplift from the 25 Cascadia source scenarios ranged from nearly 17 to  $\sim 2$  m at the latitude of Cannon Beach (Fig. 16). We also simulated inundation from the 12 Cascadia sources of the TPSW (2006) (Fig. 16). Tsunami simulations thus totaled 37 and utilized post-earthquake topography to estimate inundation.

### 5.2 Cascadia tsunami inundation and water elevation

Tsunami water elevation at the shoreline (Figs. 17, 18) and inundation (Figs. 17, 19, 20) are plotted in terms of cumulative logic tree weights in order to illustrate relative confidence that each scenario covers all potential variability for Cascadia tsunamis. Logic tree

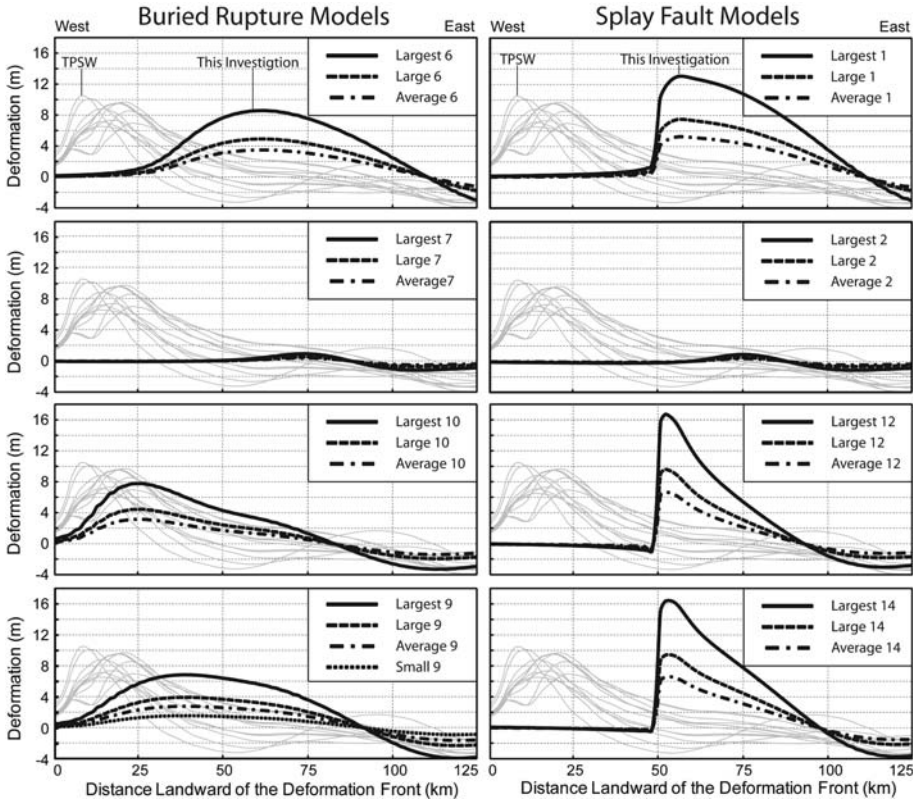


**Fig. 16** West-to-east cross sections of coseismic deformation for all Cascadia earthquake source scenarios. Cross sections extend from the deformation front to the shoreline at Cannon Beach. The final 25 tsunami sources utilized by Oregon Department of Geology and Mineral Industries (DOGAMI) for this investigation (*bold lines*) have major uplift mostly landward (east) of stochastic scenarios developed by USGS for TPSW (2006) (*thin gray lines*). Scenarios with decreasing deformation have decreasing fault slip at values of ~38, 22, and 15 m with one source scenario, Small 9, at ~8 m. Titles on each graph explain the type of slip distribution used; see also the logic tree (Fig. 10) for explanation of source scenario names in each legend

weights were summed for overlapping inundations, subtracted from 1 and multiplied by 100 to get percent confidence. We plotted results for the TPSW sources by making the ad hoc assumption that all have equal logic tree weights within their stochastic framework. TPSW tsunamis were larger than most of ours, overlapping our events at >95% confidence level (Figs. 18, 19, 20).

Water depth at the open coast for our scenario tsunamis varied from 3 to 18 m at a representative observation point (Fig. 18), while inundation varied from ~1.5 to 3.8 km in the lowest valley at Ecola Creek (Fig. 19). Runup was amplified by up to 40% at near-shore bathymetric lows, especially if combined with U- or V-shaped valleys where the ~30 m contour penetrates <1 km inland (Figs. 17, 21). Maximum open coastal runup was 30.3 m in the Tolovana area. Cascadia sources of the TPSW (2006) reached a maximum runup of 34.7 m in the same area.

Some regional slip patch sources produced inundation matching key confidence limits (Fig. 20). A summary of runup for key source scenarios designated by their names in the

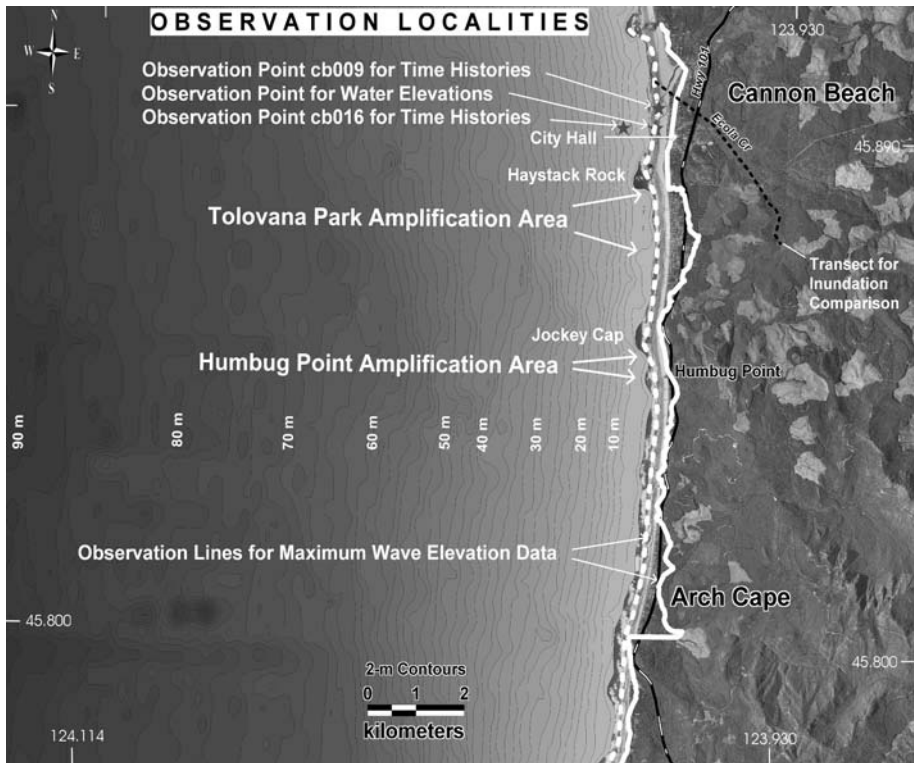


**Fig. 17** Observation lines and points for inundation, maximum wave elevations, and time histories of wave arrivals. *Solid white observation line* for maximum wave elevation data approximates the limit of inundation on steep slopes at the open coast; *dashed white observation line* approximates the shoreline (0.0 m NAVD88). *Thin black lines* illustrate water depth in 2-m intervals; labels on depths are relative to the NAVD88 datum

logic tree is given here. Approximately matching isolines of percent confidence are also listed next to each scenario name. Runup elevations are representative of most open coastal sites in the study area with maximum values in parentheses:

- Largest 14 (~99% isoline): ~20 m runup (30.3 m)
- Large 14 (~90% isoline): ~13 m runup (15.9 m)
- Average 14 (~70% isoline, preferred scenario): ~10 m runup (12.2 m)
- Average 9 (~50% isoline): ~8 m runup (9.4 m)
- Small 9 (~6–10% isolines): ~5.5 m (6.1 m)

These regional slip patch scenarios should produce inundation at approximately these confidence limits in areas north and south of Cannon Beach, because source deformation is similar. Inundation and open coastal wave elevation from the preferred source scenario, Average 14, closely tracks both the 70% confidence limit and the regulatory inundation line (Olmstead 2003) established by Oregon in 1995 (Priest 1995; Figs. 18, 19, 20). Less accurate 1995 topographic data and lack of numerical modeling in 1995 of dry land inundation probably caused most of the differences between the Average 14 and regulatory inundation, because the two simulations have similar tsunami elevations at the open coast.

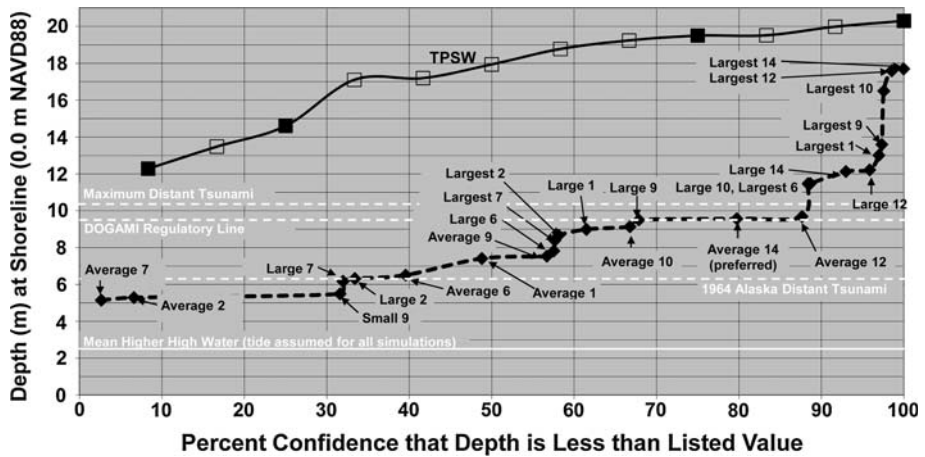


**Fig. 18** Cumulative percent confidence that tsunami water depth will be less than the scenario depth for a Cascadia tsunami (~500-years event). Average 14 is the preferred scenario that received the highest logic tree weight for the full 32-scenario analysis. Water depths of the maximum distant tsunami scenario (Source 3 of TPSW 2006), the 1964 Alaska distant tsunami, tsunami water elevation for the Oregon Department of Geology and Mineral Industries (DOGAMI) regulatory zone (Priest 1995; Olmstead 2003), and tide assumed for all simulations are shown for comparison. Included for comparison are data for the 12 stochastic sources utilized by the TPSW (2006); each is assumed to have one-twelfth of the total logic tree weight of 1.0. Note: TPSW water depths shown by open squares are inferred from results of an earlier version of the SELFE hydrodynamic model compared to four 2008 simulations (*solid squares*). All tsunami water depths are from a point located on the open coastal shoreline at 123.966586° West Longitude, 45.891190° North Latitude at approximately 0.0 m elevation NAVD88 (water level observation point in Fig. 17)

### 5.3 Effect on inundation and runup of slip, splay faulting, and slip patches

Slip magnitude was the most important control of inundation and runup, both of which increased linearly with slip (Fig. 22). The next largest differences between scenarios were caused by increasing uplift through splay faulting and distributing slip into regional versus local bank or basin slip patches (Fig. 23; Table 4). Local basin slip patches produced much smaller runup and inundation relative to all other sources (Table 4), because the nearest basin is ~100 km south of Cannon Beach (Fig. 8).

While the splay fault amplified tsunamis relative to buried rupture sources, the truncation of slip distributions at the surface trace of the splay caused the degree of amplification to decrease as more of the slip distribution was seaward of the splay (Fig. 23). Amplification by splay faulting was 6–31% for tsunami water level at the open coast and 2–20% for inundation up Ecola Creek (Fig. 23). Amplification was negligible for basin slip patches, owing to negligible slip in deep water. For sources with significant slip, amplification was largest for symmetrical regional slip patches, followed by bank slip patches, and least for seaward-skewed regional slip patches (Fig. 23).

### 5.4 Alaska 1964 tsunami simulation

Simulated open coastal runup for the 1964 Alaska tsunami was mostly ~6.5 m with a maximum of 8.2 m where the wave was funneled into the mouth of Ecola Creek. Flow depth and inundation from the simulation closely matched observations gleaned from

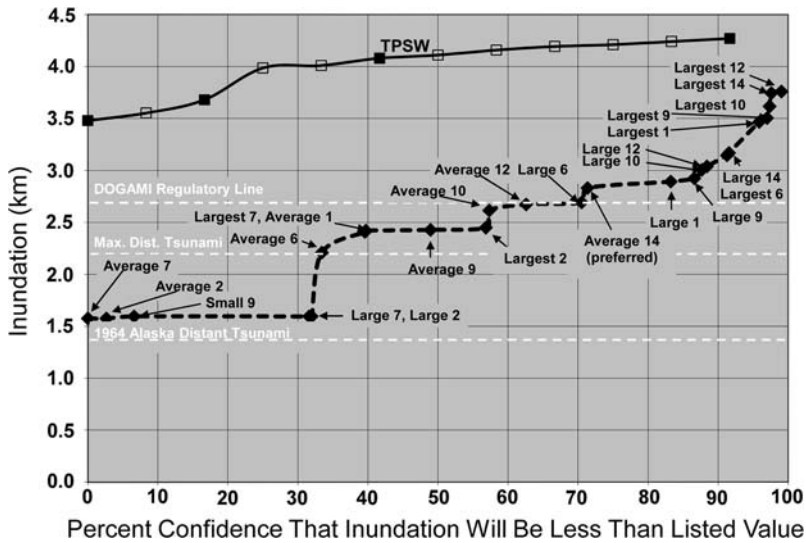


**Fig. 19** Inundation up the Ecola Creek channel versus cumulative percent confidence that inundation will be less than the listed value. Data for Cascadia sources of this investigation are on the *black dashed line*; data for source scenarios of the TPSW (2006) are on the *solid line*. Inundation for the TPSW scenarios is inferred from four 2008 simulations (*solid black squares*) and scaling linearly between these four inundations and corresponding open coastal water levels estimated from a 2007 version of the SELFE hydrodynamic model (*open black squares*). Also shown for comparison are maximum inundation from the 1964 Alaska tsunami and maximum-considered distant tsunami from the Gulf of Alaska (Source 3 of TPSW 2006). Av = average; Max. = maximum; Dist. = distant. Line of observation is indicated by the dashed black line in Fig. 17

historical records (Witter 2008) (Table 5; Fig. 24). The Bell Harbor Motel and the Steidel House had particularly high quality observational data (Witter 2008) and the best match of simulation to observations (Table 5). Match to observed inundation was improved in two trials by refining the part of the numerical grid defining the Ecola Creek channel and highway embankments. In front of the foredune in downtown Cannon Beach, the 1964 tsunami runup reached an estimated elevation of 6.1 m (NAVD88); the simulation predicted 6.7 m. Simulated inundation on the landward side of the foredune is slightly less than that estimated from historical accounts (Fig. 24), but the historical observations are highly uncertain in this area (Witter 2008). There also have been some alterations to the landscape in this same area since 1964 (Witter 2008). Considering uncertainties in geometry of the Prince William Sound earthquake source, possible nonlinear effects of tidal flow, and the 0.3 m higher tide in the simulation versus the 1964 tide, the simulated and observed inundations are remarkably close.

### 5.5 Maximum-considered distant tsunami simulation

Open coastal water elevation for the maximum-considered Gulf of Alaska tsunami was similar to Cascadia splay fault scenarios, Average 12 and 14 (Fig. 18). Open coastal runup averaged ~11 m with a maximum of 12.4 m in the Tolovana area, the same area that amplified Cascadia tsunamis. Inundation of Ecola Creek was lower than for most of the Cascadia scenarios (Fig. 19).

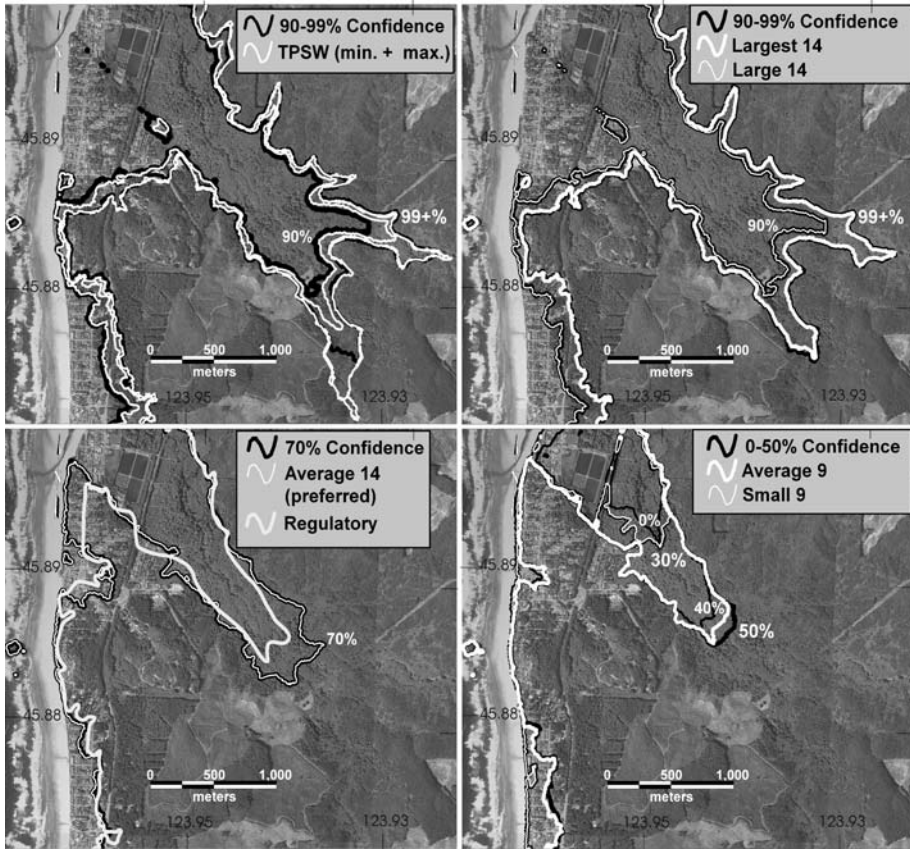


**Fig. 20** Relationship between isolines of percent confidence and key inundation boundaries. The isolines depict confidence that inundation for a Cascadia tsunami with ~500-years recurrence will be less than the isoline. *Upper left* map illustrates extension of largest TPSW scenarios past the largest inundation of this investigation (99% isoline). The minimum inundation from TPSW sources is also plotted on the *upper left* map and approximates the 96% inundation line (not plotted). *Upper right* map shows the close correspondence of scenario Large 14 (source with ~22 m slip) to the 90% isoline and scenario Largest 14 (~38 m slip) to the 99% isoline. *Lower left* map demonstrates the exact correspondence of the 70% isoline with scenario Average 14 (“preferred” source with ~15 m slip) and similarity of both to the tsunami regulatory line affecting the building code in Oregon. *Lower right* map illustrates the relationship between isolines and inundation from the scenario Average 9 (~15 m slip on buried subduction zone rupture) and the Small 9 source (~8 m slip)

### 5.6 Time histories

Timing of tsunami arrival is dependent on nearness of offshore uplift. The first tsunami peak is the largest wave in all of the Cascadia scenarios of this investigation, arriving between 24 and 34 min after the earthquake for bank and regional slip patch sources (Figs. 25, 26, 27). Basin slip patch sources have a peak arrival of ~40 min (Figs. 25, 26, 27). For the regional slip patch scenarios, the splay fault tsunami peaks arrive earlier than equivalent buried rupture cases (Fig. 28), because the buried ruptures have peak uplifts west of the splay fault (Fig. 16). Peak water levels for tsunami scenarios of TPSW (2006)

## Tsunami Elevation Along the Shoreline

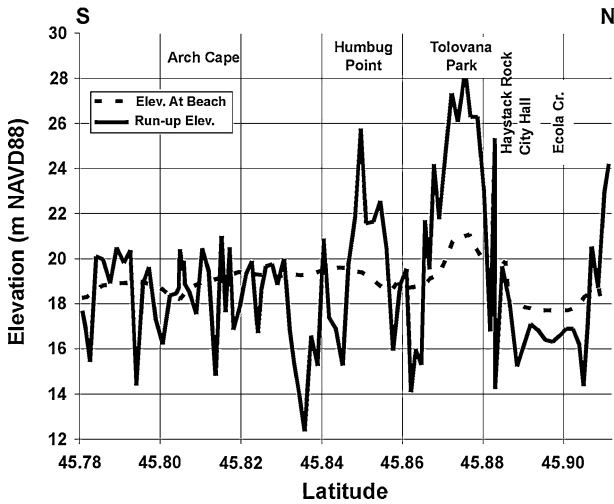


**Fig. 21** North–south variation of open coastal tsunami wave elevations for scenario largest 14, approximating the 99% isoline for all potential Cascadia tsunamis. Locations of observation lines are shown in Fig. 17. Run-up elevations are sometimes lower than maximum wave height at the beach because the elevations are taken near the limit of inundation on coastal bluffs where the water level decreases inland. In the vicinity of Ecola Creek, the “Run-up” elevation is actually the maximum wave height above the open coastal foredune (Fig. 17). Actual maximum elevations may differ slightly from these values because they are based on a cross section through a numerical grid that averages data using a nearest neighbor approach

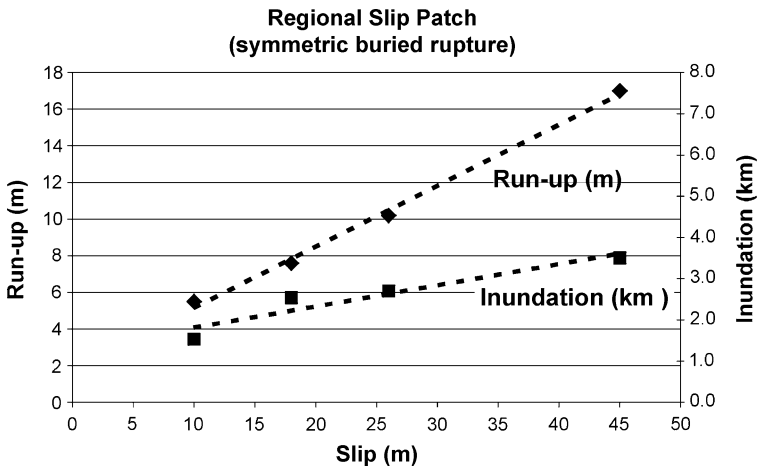


**Fig. 22** Linear relationship between fault slip and tsunami inundation or tsunami elevation at the shoreline (0.0 m NAVD88). Tsunami elevation at the shoreline is labeled “run-up” on the graph. Water elevations are measured at observation point cb009 on Fig. 17; inundation is measured along the transect shown in Fig. 17

are a few minutes later than most of our Cascadia tsunamis (Fig. 26), because peak uplifts are further offshore (Fig. 16).

The first rise of water level at the shoreline occurs sooner for wider ruptures, regardless of the location of peak uplift. Larger slip produces larger uplift over a wider area (Fig. 16),

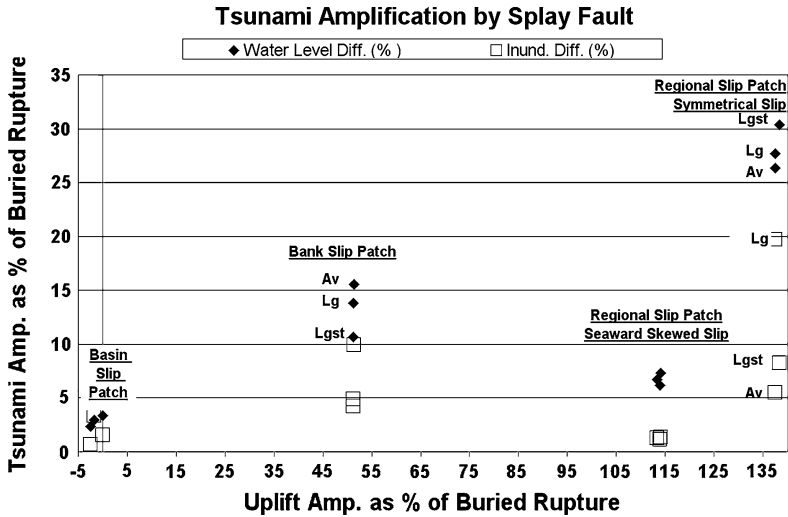


**Fig. 23** Percent amplification of water level at the shoreline and inundation up Ecola Creek by the splay fault relative to buried rupture source versus percent amplification of seafloor uplift by the splay fault. Observation point cb009 for water elevation and observation line for inundation are shown in Fig. 17. Av = average (~15 m slip); Lg = large (~22 m slip); Lgst = largest (~38 m slip)

**Table 4** Tsunami water elevation and inundation differences between regional versus local (bank or basin) asperities and splay fault versus buried rupture scenarios

Scenario	Rupture type	Slip patch type	Maximum slip (m)	Maximum offshore uplift (m)	Maximum offshore subsidence (m)	Open coastal water Elev. (m NAVD88)	Maximum inundation at Ecola Creek (km)
Average 1	Splay fault	Local bank	~15	5.3	-1.3	8.5	2.4
Average 2	Splay fault	Local basin	~15	0.4	-0.4	5.3	1.5
Average 6	Buried fault	Local bank	~15	3.4	-1.3	7.7	2.2
Average 9	Buried fault	Regional	~15	2.8	-1.6	7.6	2.5
Average 14	Splay fault	Regional	~15	6.7	-1.5	9.8	2.7

All source scenarios for this table utilize an “average” maximum slip corresponding to 525 years of convergence on the Cascadia subduction zone. Observation point cb009 for water elevation and observation line for inundation are shown in Fig. 17. Only maximum offshore or coastal uplift and subsidence is listed, because inland deformation has no effect on the tsunami inundation or run-up. Elev. = elevation

hence Cascadia source scenarios with identical slip distribution but increasing slip produce tsunamis with decreasing arrival time for first rise of water (Fig. 28). Local bank slip patches always produce the earliest first rise of water, similar to increasing rupture width of the regional slip patch by 20 km (Fig. 25), because the uplifts extend further toward the shore than the regional slip patches (Fig. 16). For example, bank slip patches with the largest slip cause a 3-m rise in shoreline water elevation only 10 min after the earthquake versus 17–23 min for regional slip patches (Fig. 27).

Offshore coseismic subsidence causes a leading depression wave, which can amplify run-up (Tadepalli and Synolakis 1994), but none of our scenarios were strongly affected by this phenomenon. Scenarios with seaward skew of slip (scenarios 10 and 12) and the basin

**Table 5** Comparison of observed water depths and elevations during the 1964 Alaska tsunami at Cannon Beach, Oregon to results of tsunami simulations; elevation of simulation in parentheses is tsunami elevation nearest to an observation point that was dry in the simulation; “<” symbol indicates that simulation was less than this ground elevation at the observation point

Site	Tsunami flow observations		Simulation results	
	Depth (m) <sup>a</sup>	Elevation, NAVD 88 (m) <sup>b</sup>	Depth (m)	Elevation, NAVD 88 (m)
Bell Harbor Motel	1.5	6.2	1.6	6.2
Steidel House	0.8	5.8	0.8	5.9
3rd & Spruce St.	0.3	5.6	0	<5.3 (~4.2)
2nd & Spruce St.	0.3	3.8	0.3	3.8
1st & Spruce St.	0.3	4.1	0.1–0.3	3.8

<sup>a</sup> Water depth estimates based on eyewitness observations noting water damage and water marks on buildings and depth of flooding along the main street in downtown Cannon Beach (Witter 2008)

<sup>b</sup> Minimum water level elevation estimate relative to the mean lower low water (MLLW) tidal datum is equal to the sum of the observed water depth and the NAVD 88 elevation of the site

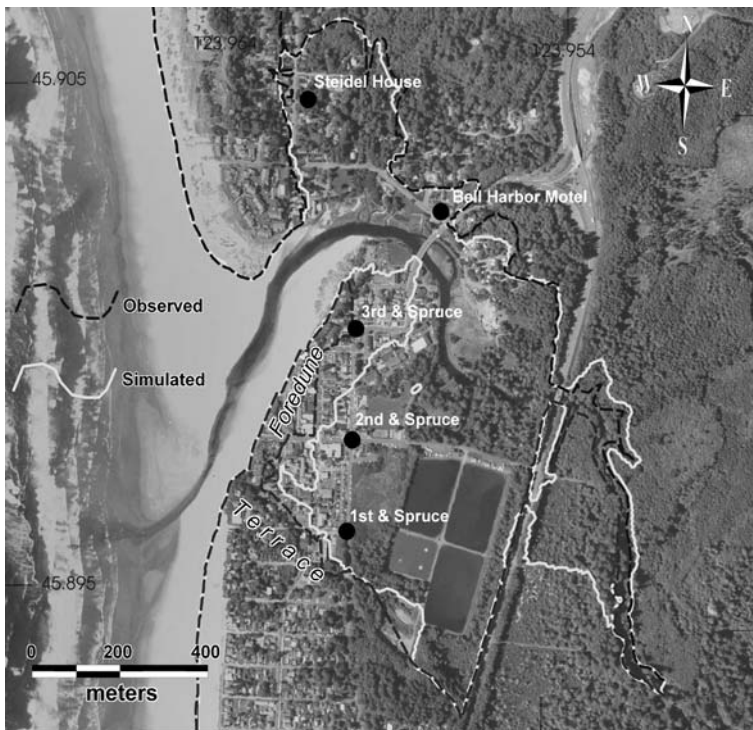


**Fig. 24** Simulated versus observed inundation from the 1964 teletsunami at Cannon Beach. Steidel House and Bell Harbor Motel are localities with high quality estimates of tsunami flow depth. Observed inundation on the east side of the foredune is highly uncertain and based on estimates of flow depth near the creek channel

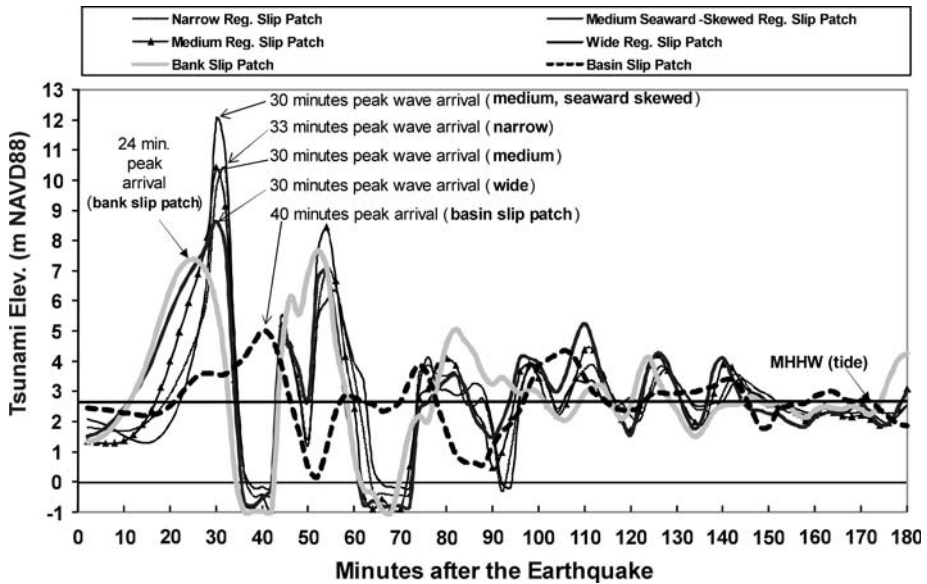


**Fig. 25** Sensitivity of wave arrival at Cannon Beach to Cascadia fault rupture width and slip distribution for splay fault scenarios with “average” slip of 15 m. The “wide” and “narrow” regional ruptures are regional slip patches with symmetric slip but rupture width increased or decreased by 20 km, respectively. MHHW = mean higher high water = 2.71 m NAVD88. MHHW is the tidal level for all simulations. Note how all simulations start with some degree of instantaneous drop in water level. This drop is caused by coseismic subsidence from the earthquake source scenario. Both the earthquake deformation and MHHW tide are initial conditions for simulations. Data are from near the open coastal shoreline (Station cb009, Fig. 17). Simulations utilize an early fault dislocation model (fb76 slip distribution without the modification by Wang and He 2008) and an early version of the SELFE hydrodynamic model, so elevations and arrival times are slightly different from those used for the final inundation map

slip patch sources (scenarios 2 and 7) have a small leading depression wave; all others have leading elevation waves (Figs. 26, 27). For the splay fault sources, the small leading depression wave in the seaward-skewed sources does not amplify the waves enough for them to exceed the height of the regional symmetric sources (Fig. 26).

Flow velocities at the open coast follow the same general pattern as water level variations (Fig. 29), but vary widely inland (Fig. 30). Tsunami velocity reaches a maximum when the surge plunges downhill on the landward side of foredunes fronting Ecola Creek (Fig. 30). Note that flow velocities are depth-averaged from the 3D velocity field, but since a zero bottom drag is used in the model, there is no shear in the 3D velocity field. We do not understand the details of the vertical structure, including the bottom boundary layer for overland flow; hence, the use of zero friction for conservative (high) estimates of velocity.

Both of the distant tsunamis arrive ~ 4 h after the source earthquake in the Gulf of Alaska but show contrasting patterns of wave height (Fig. 31). The maximum-considered distant tsunami arrives as a single initial peak over three times as high as the 1964 tsunami (Fig. 31). The initial surge of water from the 1964 tsunami arrives in two peaks, the first about half as high as the second with only a minor (0.2 m) withdrawal of water between. The second major surge of water arrives at about the same time for both scenarios but successive waves are out of phase (Fig. 31).

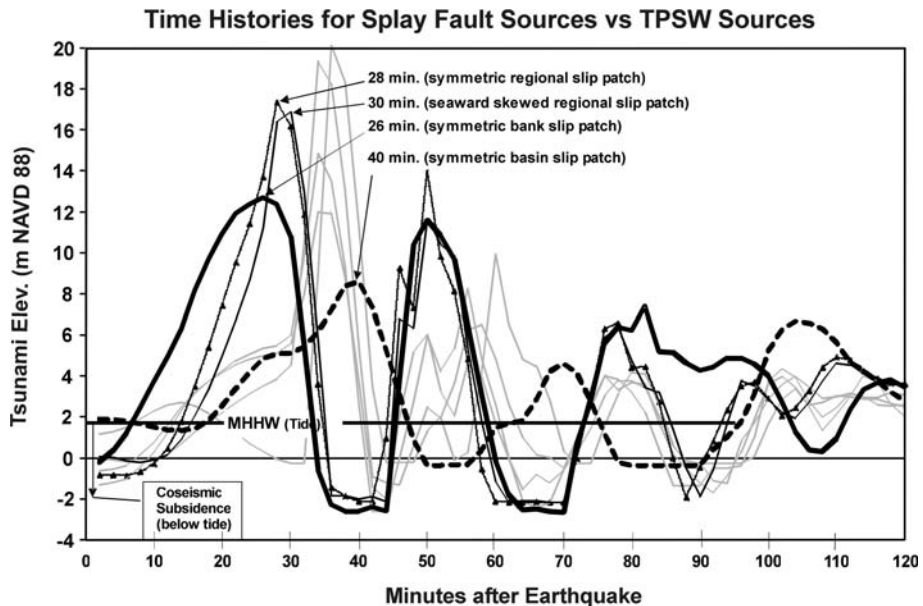


**Fig. 26** Tsunami arrival times for largest-slip splay fault sources (*bold lines*) versus earliest and latest arriving tsunamis from 12 stochastic scenarios of TPSW (2006) (*light gray lines*). All water elevations start below the prevailing tidal level owing to coseismic subsidence. Note that some water levels continue to decrease in the first 10 min after the earthquake; this indicates water withdrawal during arrival of a leading depression wave (note: because time histories for TPSW scenarios were extracted from 2007 simulations, the numerical grid and version of SELFE differs from that used for the other plotted time histories simulated in 2008; however, initial wave arrival times for 2007 simulations are within  $\pm 1$  min for 2008 simulations of the same earthquake source). Observation point is Station cb009 in Fig. 17; initial arrival times are identical within the 2-min sampling interval for locations up to 10-m water depth offshore (e.g., see time history data for point cb016 of Fig. 17 in Priest et al. 2009). Regional symmetric slip patch = Largest 14; local bank slip patch = Largest 1; seaward-skewed slip regional slip patch = Largest 12; local basin slip patch = Largest 2

## 5.7 Cascadia simulations versus paleotsunami inundation

The inland reach of the three tsunami deposits dated (Table 6) and mapped (Fig. 32) by Witter (2008) is a ground truth check for minimum inundation of past tsunamis during the last  $\sim 1,000$  years. Inundation extending beyond the maximum reach of the deposits, 1.6 km up Ecola Creek, requires at least  $\sim 15$  m of slip (recurrence of 525 years) for buried rupture sources (average 6 or 9; Fig. 32). This conclusion is unchanged whether the simulations are run with or without the foredune at the estuary mouth (Fig. 32). Other Cascadia scenarios of this investigation with tsunamis larger than the “Average” buried rupture scenarios are also consistent with paleotsunami deposits, but not with slip inferred from turbidite data (Table 1). For example, basin slip patch sources (scenarios Largest 2 and 7) require  $\sim 38$  m slip (recurrence of  $\sim 1,300$  years) to achieve inundation similar to other sources with 15 m slip (Fig. 19), but this amount of slip exceeds the T1–T4 recurrence of Goldfinger et al. (2009). Likewise, the 12 sources of the TPSW (2006) produce inundation extending past the tsunami deposits, but, all have maximum slip exceeding their average slip of  $\sim 19$  m ( $>660$  years recurrence), according to Geist (personal communication 2007).

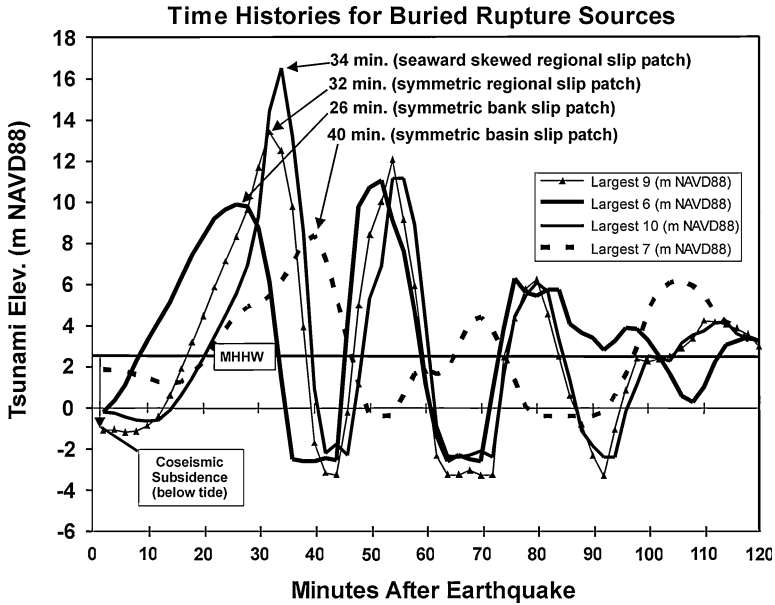


Fig. 27 Tsunami arrival times for buried rupture sources at Station cb009 in Fig. 17

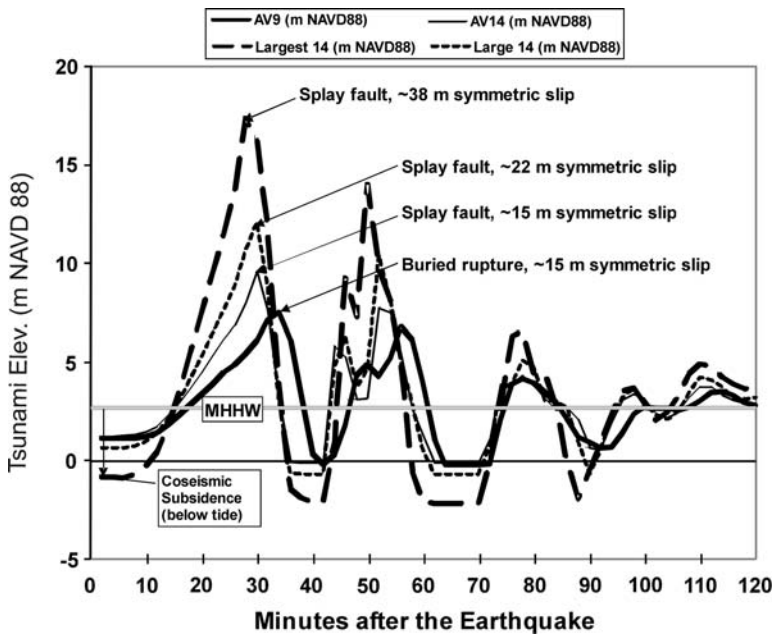
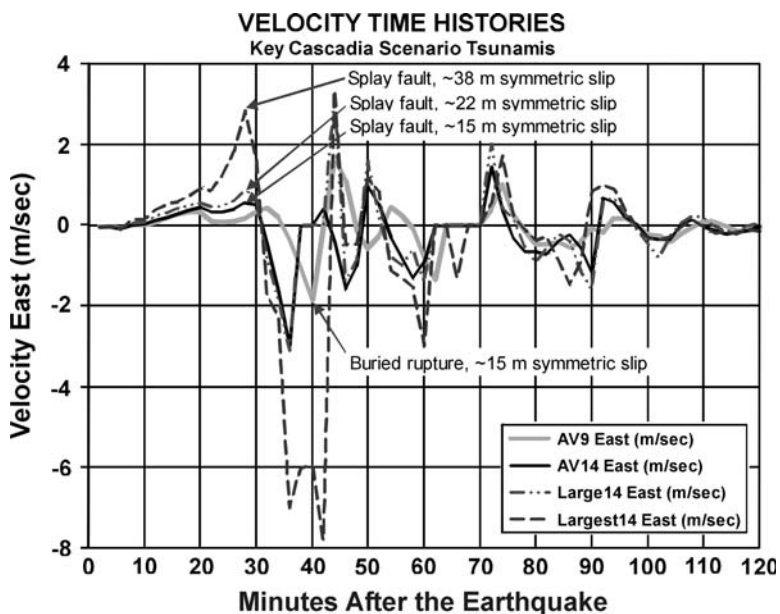


Fig. 28 Time histories of wave elevation for key regional slip patch scenarios; observation point at Station cb009 in Fig. 17. AV = average



**Fig. 29** Time histories of tsunami velocity for key tsunami scenarios at the open coastal shoreline (Station cb009 in Fig. 17). East (landward) flow is positive; west (seaward) flow is negative. One meter per second equals approximately two knots, so maximum velocities vary from  $\sim 4$  knots for scenario Average 9 to  $\sim 16$  knots for scenario Largest 14

According to interpretations of turbidite data by Goldfinger et al. (2008, 2009), Cascadia ruptures contemporaneous with the three tsunami deposits were full-margin events separated by interseismic intervals of 162–435 years (T1–T4, Table 1). However, T2 is a thin turbidite of low mass, suggesting a low slip value, if mass has some correlation to earthquake size (Goldfinger et al. 2009). We suggest that energy release in T2 was probably low, and that the slip required was in part accumulated during the interval between T3 and T1 (422–637 years, Table 1). The discrepancy could also be attributed to splay faulting or tidal level. Figure 23 demonstrates that splay fault amplification of tsunamis for this slip magnitude is only  $\sim 6\%$ , thus decreasing needed slip from  $\sim 15$  to 14 m. The assumed mean higher high water tide is already maximizing tidal amplification, so decreasing needed slip by increasing tide is unlikely. One caveat is that we did not evaluate tidal effects, especially nonlinear amplification by flood tides.

The AD 1700 tsunami deposit is the least widespread of the three mapped in Ecola Creek (Fig. 32), whereas the AD 1700 earthquake produced coastal submergence and turbidites with thickness/mass equal to or larger than the previous three events (Table 1). If coastal submergence and turbidite thickness/mass correlate with earthquake size, then some other factor must account for the mismatch. We speculate that this factor is contemporary tide. Mofjeld et al. (1997) inferred that the AD 1700 tsunami (youngest Cascadia deposit) occurred during a relatively low, neap tide all along the West Coast. We estimate from his data that the 1700 tsunami arrived at Cannon Beach on a neap tide at  $\sim 0.8$  m NAVD88,  $\sim 1.9$  m lower than our simulated static tide. On the other hand, Mofjeld et al. (1997) also point out the likelihood that tidal level could have been amplified by the common occurrence of atmospheric low pressure during the winter months. Myers

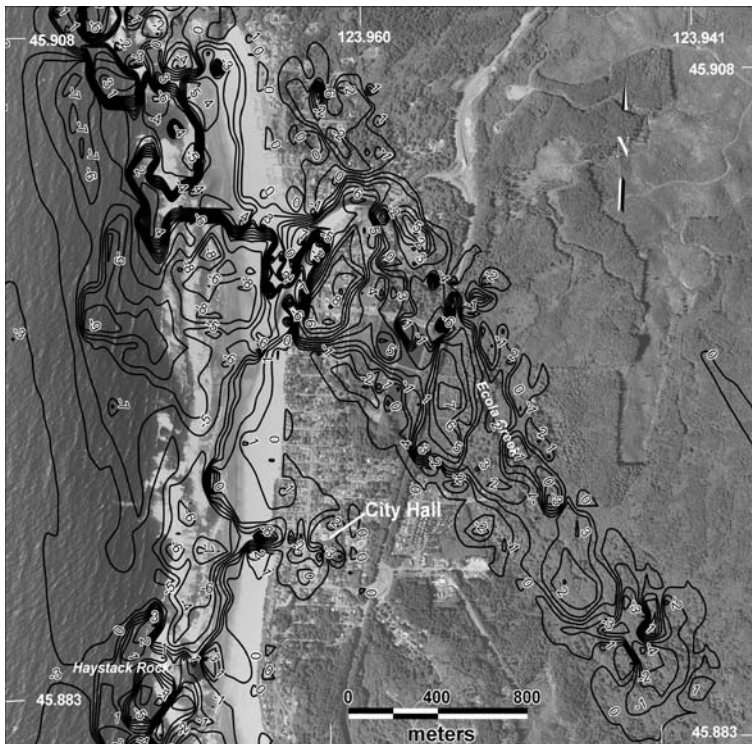


**Fig. 30** Maximum velocity map for the Average 14 (preferred) tsunami scenario, approximating the ~70% confidence level for all variability in velocity for Cascadia tsunamis; contoured at 1 m/s intervals (*black lines*); positive values = east velocity; negative values = west velocity (note: convert meter per second to knots by multiplying by 1.944; to miles per hour by multiplying by 2.237). The 0 m/s contour near the beach is an artifact of the change in direction of maximum current velocity between offshore and onshore. This contour marks the boundary where maximum current velocities of the withdrawing waves (negative values) are larger than maximum current velocities of landward surging waves (positive values)

(1999) and Myers and Baptista (2001) showed that tidal flow produces strong nonlinear effects on tsunami flow, so a withdrawing tidal current could have reduced inundation in 1700 regardless of absolute tidal height.

### 5.8 Match of coseismic subsidence to paleosubsidence

Paleoseismic subsidence for the AD 1700 event from Leonard et al. (2004) generally matches “large” to “average” slip scenarios better than “small” or “largest” slip cases (Fig. 33). The one “small” scenario utilized in the investigation, Small 9, fit the coseismic subsidence estimates of Nelson et al. (2008) for the last four Cascadia earthquakes at Alsea Bay (Waldport) which has anomalously low subsidence values (Fig. 33) consistent with low coupling in that location. The paleoseismic subsidence appears less variable from north to south than is predicted by the local slip patch scenarios (top four graphs in Fig. 33), matching regional rupture scenarios somewhat better (bottom four graphs in Fig. 33). However, the northern limit of our northernmost local bank slip patch scenario, centered on Nehalem Bank (Figs. 5, 11), is arbitrary and not defined by geophysical data

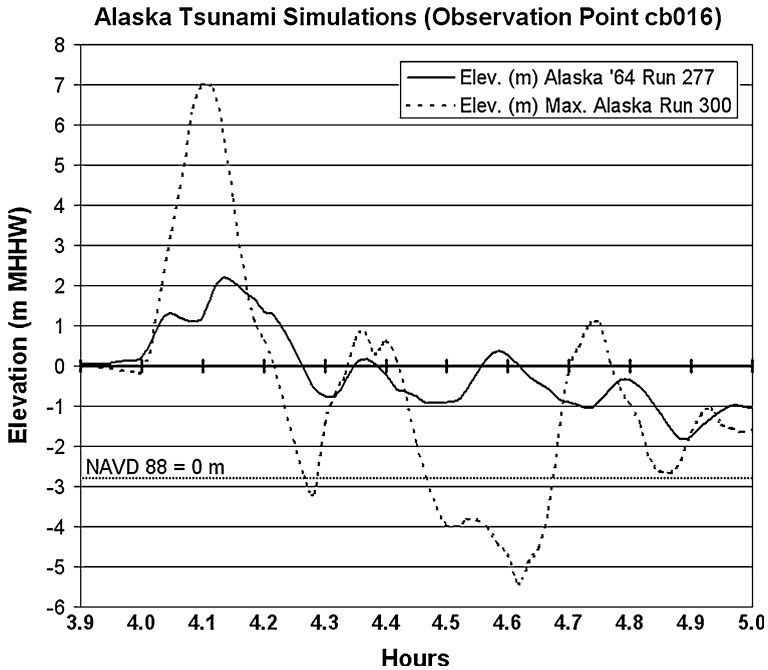


**Fig. 31** Time histories of wave elevation for the 1964 Alaska and maximum-considered distant tsunami scenarios; 5-h simulation at Station cb016 shown on map in Fig. 17. Elevations shown relative to assumed tide at mean higher high water (MHHW); the 0.0 m NAVD88 datum is shown for comparison

**Table 6** Preferred radiocarbon ages for three sand layers identified as tsunami sands at Cannon Beach; data are from Witter (2008)

Sand layer	Depth (m)	Preferred age (years before 1950) <sup>a</sup>
1	0.46	144–270 <sup>b</sup>
2	0.96–1.25	520–800 <sup>c</sup>
3	0.62–1.39	910–980 <sup>d</sup>

<sup>a</sup> Age ranges rounded to the nearest decade except for historical constraints on the estimate for sand layer 1

<sup>b</sup> Upper bound of age range constrained by the year 1806 when Lewis and Clark reached Ecola Creek and written history began in coastal Oregon

<sup>c</sup> Age range represents the sum of probabilities for both <sup>14</sup>C ages for sand layer 2. Two samples were dated and met a chi-square test that shows statistical difference at the 95% level

<sup>d</sup> Age range represents 97% of the relative area of the calibrated age distribution for the pooled mean age of three <sup>14</sup>C dates for sand layer 3. The three ages are indistinguishable based on a chi-square test for statistical difference at the 95% level

offshore. This slip patch may extend further north, or become a long regional patch as suggested by GPS and leveling data (McCaffrey et al. 2007; Burgette et al. 2007, 2009). If this is the case, fit to the bank models is improved. Most of the TPSW scenarios exceeded paleoseismic deformation along the coast (Fig. 33).

Neither the TPSW nor our scenarios closely match the pattern of paleosubidence in the east–west cross section up the Columbia River (Fig. 34). This may be due to too broad of a

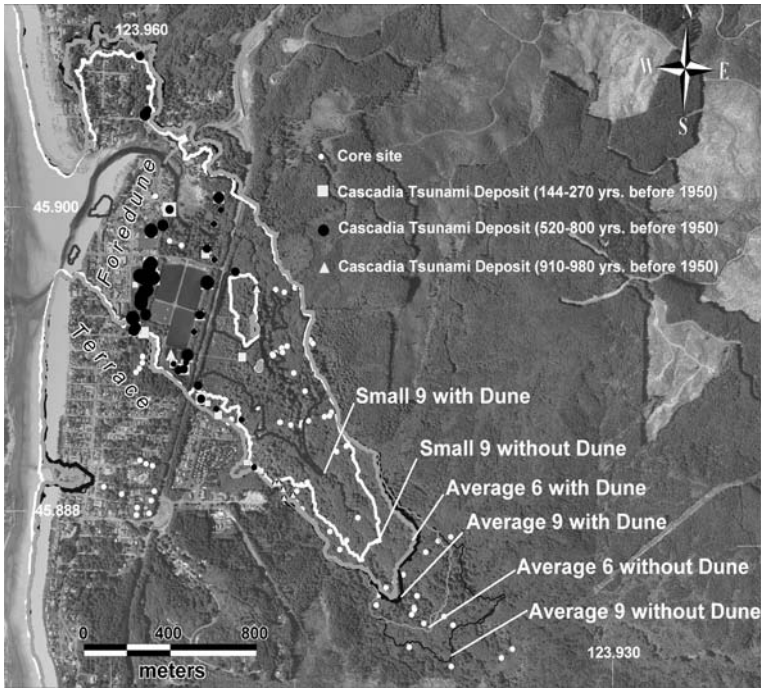


**Fig. 32** Comparison of where tsunami deposits were found in cores versus tsunami inundation simulated on a paleolandscape with and without a foredune. Size of symbols corresponds to relative deposit thickness; *white dots* are core sites with no tsunami sand. All paleotsunami data are from Witter (2008). Note that simulated inundation is ~70 m seaward of the modern coastline; this is caused by translation of the coastline seaward to account for 1,000 years of coastal retreat. Earthquake source scenarios: Small 9 = ~8 m slip, regional slip patch, buried rupture; Average 9 = ~15 m slip, regional slip patch, buried rupture; Average 6 = ~15 m slip, local bank slip patch, buried rupture

landward transition zone on the megathrust, interaction with other upper plate faults and structures, or, more likely, error in the paleoseismic data. Some of these paleosubsidence data are of low quality, according to the rating system of Leonard et al. (2004); these low quality data did not influence our construction of fault source scenarios.

## 6 Discussion

### 6.1 Uncertainty in paleoseismic estimates of coseismic subsidence

Paleosubsidence is measured in vertical soil profiles from changes of estuarine micro- and macro-fossil assemblages sensitive to local sea level, so it is possible that prompt post-seismic deformation could occur before these signals are recorded in the deposits. Post-seismic deep fault slip could increase subsidence near the coast, whereas uplift from viscoelastic relaxation could reduce it over hours, days or a few years after an earthquake (Hyndman et al. 2005; Wang 2007). Post-seismic slip can also raise the coast (Sawai et al. 2004). Decreasing salinity of estuarine waters upstream can expand downward the vertical ranges of salinity-intolerant species like Sitka Spruce that are used for subsidence

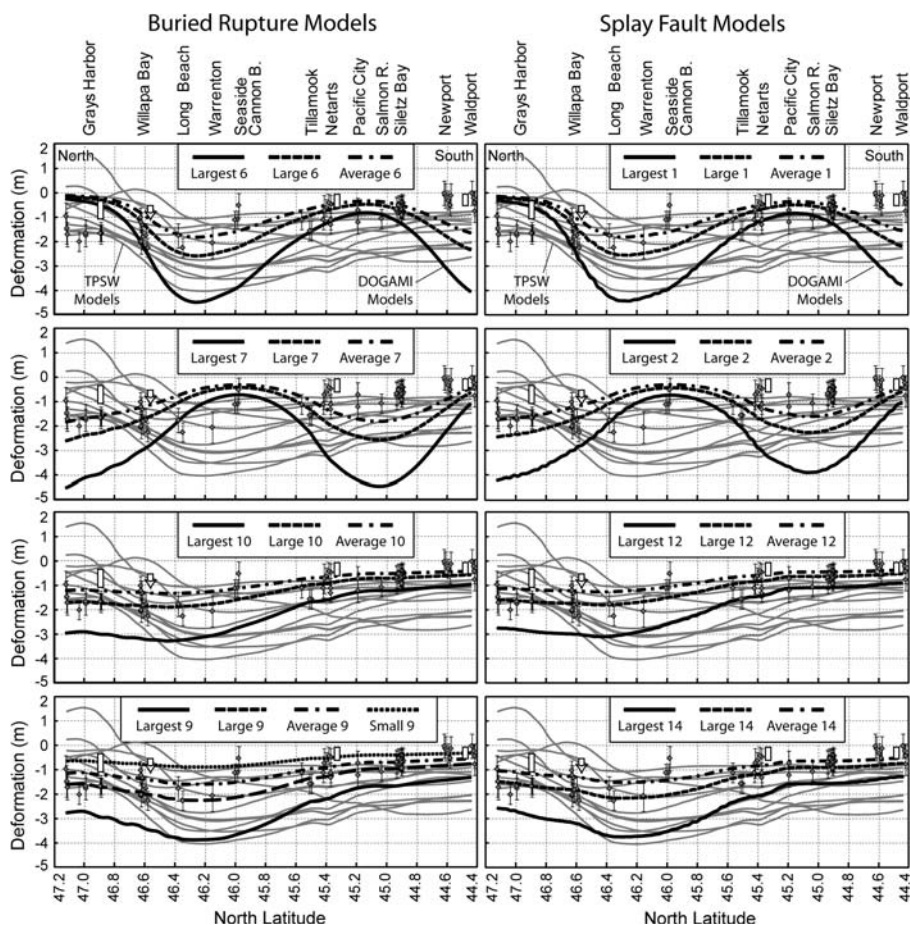


**Fig. 33** Correspondence at the outer coast of scenario coseismic deformation to paleosubsidence data for the AD 1700 Cascadia earthquake of Leonard et al. (2004) (diamonds with error bars) and Nelson et al. (2008) (open bars; one open arrow indicating that value is a minimum for the locality). Deformations shown as gray lines are from Cascadia earthquake sources S1–S12 of the TPSW (2006) investigation; black lines are sources of this investigation (labeled “DOGAMI models” in top charts). Note that many TPSW deformations have subsidence larger than the AD 1700 data as do many of the “Largest” scenarios of this investigation. B. = beach; R. = river; DOGAMI = Oregon Department of Geology and Mineral Industries

estimates; this factor may be the principal reason much of the paleosubsidence data from the Columbia River exceed our source scenarios.

## 6.2 Uncertainty in paleoseismic recurrence (fault slip)

The four recurrence intervals used to define small, average, large, and largest slip scenarios were picked in 2007 from turbidite ages available at that time. While uncertainty inherent in the dating techniques is on the order of  $\pm 100$ – $300$  years at  $2\sigma$ , new age data and analysis became available during the course of the investigation, leading to mismatches between 2007 and 2009 data. Changes were generally minor for all but the largest recurrence intervals, which, as previously explained, were the most difficult to date (see

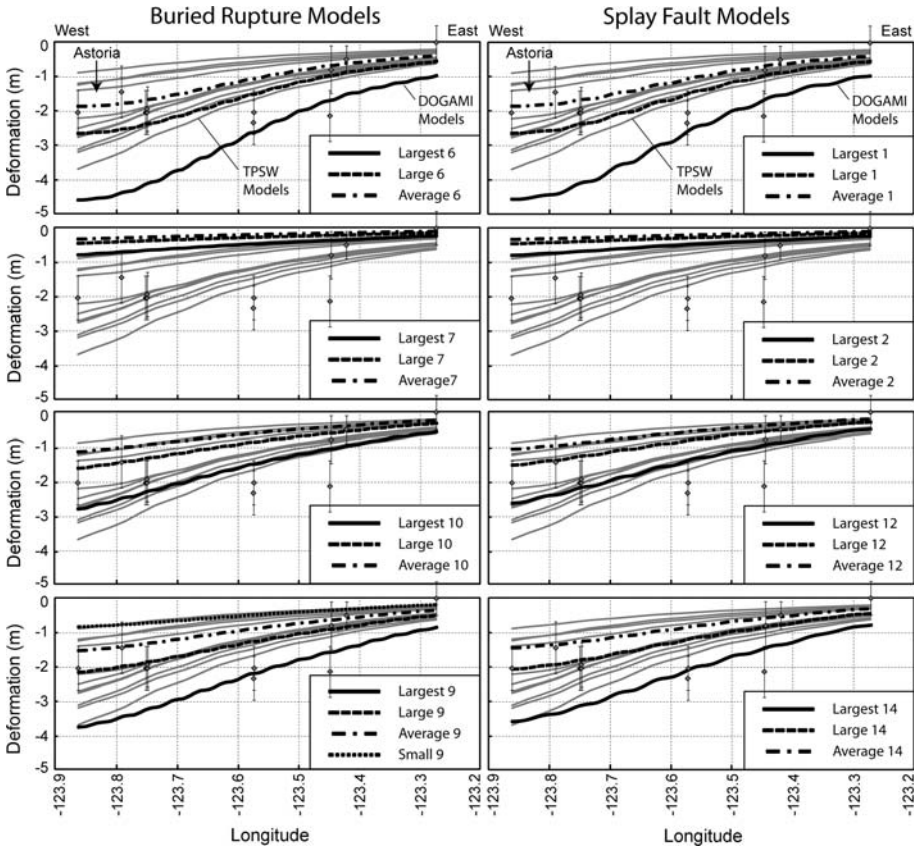


**Fig. 34** Correspondence from Youngs Bay east along the Columbia River of scenario coseismic deformations to paleosubsidence data of Leonard et al. (2004) for the AD 1700 Cascadia earthquake (diamonds with error bars). Deformations shown as gray lines are from Cascadia earthquake sources S1–S12 of the TPSW (2006) investigation; black lines are sources of this investigation

Priest et al. 2009 for detailed discussion). The largest mean recurrence in 2007 was 1,298 years ( $2\sigma$  range of 1,110–1,440 years), leading to use of this interval for the largest slip. This interval is still within the  $2\sigma$  root mean square error of the largest recurrence in Table 1 for full-margin events (i.e., without event T5b), but must be viewed as a highly conservative scenario.

Mismatches between turbidite size and the prior or following intervals indicate caution in adopting individual intervals as a metric for the largest event. Because the correlation of turbidite size to time between turbidites is only a modest one (Goldfinger et al. 2009; Priest et al. 2009), strict adherence to these times is not warranted. Furthermore, evidence suggests that smaller events use very little energy, and skew the interevent time values inappropriately. For example, event T12 was preceded by  $\sim 850$  years ( $2\sigma$  range of 584–1,115 years), and followed by 700 years ( $2\sigma$  range of 410–986 years), yet it was the smallest-mass turbidite of those considered here (Table 1). The  $\sim 1,550$  year interval ( $2\sigma$  range of 1,283–1,808 years) between T13 and T11 represents  $\sim 45$  m of plate motion, yet only turbidite T12 occurred during that period. We suspect that much of that strain was released in the earthquake that caused one of the largest turbidites, T11, though the preceding and following times for T11

---

were not extraordinary. As previously discussed, we came to similar conclusions when comparing simulated inundation to distribution of Cascadia tsunami deposits. The small-volume turbidite, T2, provided a very short minimum interevent time (slip) that would be inconsistent with observed tsunami deposits. We conclude that use of any turbidites as small as or smaller than T2 for calculation of interseismic intervals likely causes underestimation of slip. If this is the case, then we might ignore T12 in the T11–T13 interval and assign a maximum interseismic time of 1,550 years rather than 1,300 years. Viewed in this context, 1,300 years is not overly conservative.

Our assumption that the coupling ratio is 1.0 for calculation of maximum slip from recurrence data probably overestimates potential slip to some extent. McCaffrey (1997) argues that the closest subduction zone analogues to Cascadia in terms of thermal regime have a large component of aseismic slip (coupling ratio <1.0). He suggests that much of the slip release at Cascadia could be in the form of “slow earthquakes” that would greatly reduce seismic shaking. He explains the observation by Satake et al. (2003) that a large Cascadia earthquake caused the AD 1700 tsunami by calling on slow earthquakes that can produce significant tsunamis but little seismic shaking. Depending on how much slip is too slow to be tsunamigenic, we could be overestimating tsunamigenic slip based on interevent times.

### 6.3 Uncertainty in the local basin and bank slip patch sources

Wells et al. (2003) hypothesized that higher coseismic slip will be centered under forearc sedimentary basins and used gravity lows as a proxies for these basins. In Oregon, Nehalem Bank was predicted as one of these slip patches, but it is both a structural high and a gravity low. This apparent contradiction is due to youthful development of the bank from recently re-accreted materials from the local Columbia River source (Kulm et al. 1973). We modified our sources such that the bank is an area of low slip in our basin slip patch source to be consistent with the basin model proposed by Wells et al. (2003). Alternatively, if the gravity signature is important apart from being a basin proxy (Song and Simons 2003), then our local slip patch model does not capture that possibility, one for which there is no clear physical explanation.

### 6.4 Uncertainty in the fault dislocation model

The Wang and He (2008) fault dislocation model, as applied here, does not allow significant slip near the deformation front owing to the velocity-strengthening assumption, but there is some uncertainty about this assumption. According to Wang and He (2008) there is speculation that, in the course of the evolution of pore fluid pressure distribution, parts of the up-dip segment at some subduction zones may occasionally become moderately velocity-weakening and, when triggered to slip, acquire tsunamigenic rupture speed (Seno 2002). Earthquakes characterized by this type of coseismic slip are “tsunami earthquakes” with relatively high slip near the deformation front, low felt shaking, and produce relatively large tsunamis. While we cannot rule out these earthquakes on the Cascadia subduction zone, the widespread occurrence of turbidites offshore (e.g., Goldfinger et al. 2003a, 2009) and liquefaction features onshore (Obermeier and Dickenson 2000) is consistent with at least moderate coseismic ground motion over wide areas for the vast majority of Cascadia events. Additional slow slip of the outer wedge remains a possibility.

There is also significant uncertainty about the down-dip extent of coseismic ruptures. Some of this uncertainty is demonstrated by up to ~25 km mismatch between the lateral

position of the modeled down-dip extent and the “stress line” (Fig. 8) that came about from trials that matched modeled subsidence to paleosubsidence data of Leonard et al. (2004). Szeliga et al. (2008) found from inversions of geodetic data that the preponderance of slow slip events on Cascadia takes place down dip of the 25-km depth contour on the subducting plate. Our modeled down-dip extent approximates the 25-km depth contour (Fig. 8), but insufficient observation time has elapsed for these geodetic data to assess whether slip in the lower part of the megathrust interface reduces plate convergence strain as fast as it accumulates on the locked zone (Szeliga et al. 2008). More importantly, the geodetically inferred down-dip limit of interseismic locking can be very different from the down-dip limit of coseismic rupture because of the viscoelastic behavior of the system (Wang et al. 2003). In view of the rather small differences in tsunamis generated by  $\pm 20$  km in rupture width (Fig. 25) uncertainty in rupture width is at best a second order concern.

### 6.5 Uncertainty in the hydrodynamic model

The hydrodynamic model, SELFE, passed all standard tsunami benchmark tests (Zhang and Baptista 2008) and closely reproduced observed inundation and flow depths of the 1964 Alaska tsunami in Cannon Beach, thus we have considerable confidence in the code. The model was run with zero friction, so it probably overestimates inundation somewhat, although match of the simulated and observed inundation for the 1964 tsunami in developed areas indicates that the overestimate may be small where heavy vegetation is not present. We can speculate that degree of overestimate probably depends on how far inundation proceeds and how many obstacles the flow encounters. In low lying areas like the Ecola Creek valley where closely spaced trees and other vegetation could slow tsunamis, the overestimate could be significant. The practical significance is that the minimum coseismic slip of  $\sim 14$ – $15$  m for inundation beyond paleotsunami deposits may be somewhat larger than inferred here. A further practical result is that inundation at a particular confidence limit is at a maximum for that limit. A full analysis of the friction parameters relative to empirical observations was beyond the scope of this investigation.

### 6.6 Tsunamis from southern Cascadia earthquakes

In this investigation, we do not consider segment ruptures of the Cascadia subduction zone in southern Oregon. Cannon Beach is north of inferred southern Oregon segment ruptures (Goldfinger et al. 2008, 2009), and would not be expected to experience significant tsunamis from such events, given the directivity of tsunami energy away from the long axes of seismic sources (Titov et al. 1999). One caveat on this expectation is the conclusion of Myers (1999) that tsunami energy is more efficiently radiated north from southern segment ruptures than south from northern ruptures on the Cascadia subduction zone.

### 6.7 Key observations

Lack of local historical observations of Cascadia tsunamis creates high uncertainty in estimation of the hazard, but parametric analysis of geologically reasonable coseismic deformations allows quantification of this uncertainty. Simulated Cascadia tsunami elevation and inundation varied linearly with fault slip, thus understanding how much slip is reasonable is critical. Paleoseismic estimates of earthquake recurrence were thus the key constraint on tsunami hazard. Maximum runup for Cascadia tsunamis varied from 9 to 30 m, but tsunamis

---

approaching 30 m required  $\sim 38$  m of slip, an event that may have happened only once in the last 10,000 years, according to interseismic intervals inferred from turbidite data. Minimum slip of 14–15 m on the Cascadia subduction zone is needed to produce tsunamis large enough to cover the three tsunami sands deposited over the last  $\sim 1,000$  years at Cannon Beach. Arrival times of tsunami wave peaks varied little among the 25 Cascadia source scenarios (26–34 min), but the time of first significant (3-m) rise of water elevation at the shoreline was lower (10 min) for slip patches confined to submarine banks relative to regional slip patches (17–23 min). Amplified uplift on a splay fault caused up to 31% increase in runup and up to a 20% increase in inundation, so accurate depiction of splay faults is also critical. Cascadia fault rupture models that placed slip patches on a regional Cascadia locked zone or on local submarine banks were most consistent with available geodetic, paleosubsidence, paleotsunami, geological, and geophysical data. Cascadia sources with fault slip confined to forearc basins or with slip skewed seaward from a symmetrical distribution (e.g., scenarios of TPSW 2006) were less consistent with these data.

Perhaps the most useful product of this work is providing confidence levels that Cascadia inundation will not exceed certain elevations or mapped boundaries. For example, the 99th percentile inundation line for Cascadia sources is at nearly twice the elevation of the 90th percentile line in most areas of Cannon Beach.

Resources were inadequate to do a complete parametric analysis of all distant tsunami sources, so we simulated only two maximum-considered events. The hydrodynamic simulation matched observed inundation from the largest historical distant tsunami, the 1964 Gulf of Alaska event, with open coastal runup of  $\sim 6.5$  m (maximum of 8.2 m). Open coastal runup of  $\sim 11$  m (maximum of 12.4 m) from a hypothetical maximum-considered Gulf of Alaska event was similar to the “preferred” Cascadia scenario (highest logic tree weight) at  $\sim 10$  m (maximum of 12.2 m).

## 7 Conclusions and recommendations

This paper illustrates a useful technique for estimation of tsunami hazard posed by a local subduction zone earthquake where considerable geological and geophysical data exist. We demonstrate that differences in source geometry cause large differences in resulting tsunamis, underlining the critical importance of accurate, geologically reasonable tsunami source characterization. Historical and prehistorical (paleotsunami) observations provided ground truth checks of the approach. The chief parameters controlling Cascadia tsunami size from most to least important are megathrust slip magnitude, enhanced uplift from a splay fault, rupture extent, and distribution of slip. Twenty-five Cascadia earthquake sources and resulting tsunami simulations adequately explored the variation of local tsunami hazard to the Washington and northern Oregon coast. Ideally, tsunami hazard assessments for this region would employ all 25 sources to produce percentile inundation lines that express the confidence level (percentage) that a Cascadia tsunami will *not* exceed each line. However, if simulation of all 25 sources is not possible, an adequate assessment at other nearby sites may be accomplished with fewer sources drawn from this study (see Priest et al. 2009, for digital source deformation data). The five sources that best represent Cascadia source variability are

1. Scenario Average 9, regional Cascadia slip patch on a buried rupture, produces minimum inundation consistent with the last three Cascadia tsunami deposits; produces inundation encompassing  $\sim 50\%$  confidence limit.

2. Scenario Average 14, regional Cascadia slip patch on a splay fault, has highest logic tree weight; produces inundation encompassing  $\sim 70\%$  confidence limit.
3. Scenario Large 14, regional Cascadia slip patch on a splay fault, produces inundation encompassing  $\sim 90\%$  confidence limit.
4. Scenario Largest 14, regional Cascadia slip patch on a splay fault, produces inundation encompassing  $\sim 99\%$  confidence limit.
5. Either the scenario Largest 1 (local bank slip patch) or Largest 2 (local basin slip patch) scenario, whichever is the larger uplift, explores minimum tsunami arrival time.

If resources do not allow a complete parametric analysis of distant tsunamis, we recommend simulation of only one or two maximum-considered events:

1. Maximum-considered distant tsunami from the Gulf of Alaska (Source 3 of TPSW 2006) and
2. If local observational data are available, simulation of the tsunami from the 1964 Prince William Sound earthquake for ground truth check on the hydrodynamic modeling approach.

If evacuation planning is the chief objective, only two simulations need be accomplished, scenario Largest 14 and the maximum-considered distant tsunami source (source 3 of TPSW 2006). These scenarios define tsunami evacuation zones for Cannon Beach (see Cannon Beach evacuation map at <http://www.oregongeology.org/pubs/tsubrochures/CannonEvac.pdf>).

This investigation is the first phase of a state of Oregon project aimed at tsunami hazard assessment of the entire Oregon coast. The second phase is a similar detailed analysis of the Bradley Lake-Bandon area of the southern Oregon coast where subduction zone geology is significantly different and smaller Cascadia rupture lengths occur (e.g., Kelsey et al. 2005; Goldfinger et al. 2008, 2009). The latter project is expected to be complete in 2010.

**Acknowledgments** This investigation was supported by National Oceanic and Atmospheric Administration (NOAA) Requisition Number NRMAH000-6-01035 through Oregon Department of Geology and Mineral Industries (DOGAMI) Intergovernmental Agreement number 61110-09192006, and support from the City of Cannon Beach, the Cannon Beach Rural Fire Protection District, and the Seaside School District through Intergovernmental Agreement 41180-63006. The Pacific Marine Environmental Laboratory of NOAA kindly provided earthquake source data for the two distant tsunami scenarios and cooperated at every stage of the investigation. Harvey Kelsey of Humboldt State University, Vasily Titov of NOAA and Eric Geist of the US Geological Survey provided key reviews of an early draft. Brian Atwater of the USGS reviewed a later draft and offered key advice on paleosubsidence data. The authors acknowledge Western Geco and the US Geological Survey for providing some of the seismic reflection data for the purpose of this research. Angie Venturato of NOAA produced the initial compilation of topographic and bathymetric data. Charles Seaton of the OGI School of Science and Engineering, Oregon Health & Science University provided key support with data reduction at all stages of the project. Ian Madin, Vicki McConnell and Don Lewis of DOGAMI provided helpful review and advice. We thank local stakeholders for their wise council and cooperation, particularly Al Aya and Cleve Rooper of the Cannon Beach Rural Fire Protection District, Richard Mays and Jay Raskin of the City of Cannon Beach, and Doug Dougherty, Superintendent of the Seaside School District.

## References

- Adam J, Klaeschen D, Kukowski N, Flueh E (2004) Upward delamination of Cascadia Basin sediment infill with landward frontal accretion thrusting caused by rapid glacial age material flux. *Tectonics* 23:TC3009
- Adams J (1990) Paleoseismicity of the Cascadia subduction zone: evidence from turbidites off the Oregon-Washington margin. *Tectonics* 9:569–583

- Allan JC, Priest GR (2001) Evaluation of coastal erosion hazard zones along the dune and bluff backed shorelines in Tillamook County, Oregon, Cascade Head to Cape Falcon, Preliminary Technical Report to Tillamook County. Oregon Department of Geology Mineral Industries Open-File Report O-01-03
- Ammon CJ, Ji C, Thio H-K, Robinson D, Ni S, Hjorleifsdottir V, Kanamori H, Lay T, Das S, Helmberger D, Ichinose G, Polet J, Wald D (2005) Rupture process of the 2004 Sumatra–Andaman Earthquake. *Science* 308:1133–1139
- Atwater BF, Nelson AR, Clague JJ, Carver GA, Yamaguchi DK, Bobrowsky PT, Bourgeois J, Darienzo ME, Grant WC, Hemphill-Haley E, Kelsey HM, Jacoby GC, Nishenko SP, Palmer SP, Peterson CD, Reinhart MA (1995) Summary of coastal geologic evidence for past great earthquakes at the Cascadia subduction zone. *Earthq Spectra* 11(1):1–18
- Atwater BF, Tuttle MP, Schweig ES, Rubin CM, Yamaguchi DK, Hemphill-Haley E (2004) Earthquake recurrence inferred from paleoseismology. In: Gillespie AR, Porter SC, Atwater BF (eds) *The Quaternary period in the United States*. *Dev Quat Sci* 1:331–348
- Atwater BF, Musumi-Rokkaku S, Satake K, Tsuji Y, Ueda K, Yamaguchi DK (2005) The orphan tsunami of 1700—Japanese clues to a parent earthquake in North America. US Geological Survey Professional Paper 1707
- Barrientos SE, Ward SN (1990) The 1960 Chile earthquake: inversion for slip distribution from surface deformation. *Geophys J Int* 103:589–598
- Burgette R, Weldon RJ, Schmidt D (2007) A more accurate vertical velocity field for coastal Oregon reveals variations in extent of locking on the Cascadia subduction zone. *Eos Trans Am Geophys Union*, vol 88 (G52A-01)
- Burgette R, Weldon RJ, Schmidt D (2009) Interseismic uplift rates for western Oregon and along-strike variation in locking on the Cascadia subduction zone. *J Geophys Res* 114:B01408. doi:10.1029/2008JB005679
- Chlieh M, Avouac J-P, Hjorleifsdottir V, Song T-RA, Ji C, Sieh K, Sladen A, Hebert H, Prawirodirdjo L, Bock Y, Galetzka J (2007) Co-seismic slip and afterslip of the great ( $M_w$  9.15) Sumatra–Andaman earthquake of 2004. *Bull Seismol Soc Am* 97(1):S152–S173
- Cummins PR, Hori T, Kaneda Y (2001) Splay fault and megathrust earthquake slip in the Nankai Trough. *Earth Planets Space* 53(4):243–248
- Dragert H, Hyndman RD (1995) Continuous GPS monitoring of elastic strain in the northern Cascadia subduction zone. *Geophys Res Lett* 22:755–758
- Fisher D, Mosher D, Austin JA, Gulick SPS, Masterlark T, Moran K (2007) Active deformation across the Sumatran forearc over the December 2004  $M_w$  9.2 rupture. *Geology* 35:99–102
- Flück P, Hyndman RD, Wang K (1997) 3-D dislocation model for great earthquakes of the Cascadia subduction zone. *J Geophys Res* 102:20539–20550
- Freund LB, Barnett DM (1976) A two-dimensional analysis of surface deformation due to dip-slip faulting. *Bull Seismol Soc Am* 66:667–675
- Global Centroid Moment Tensor Database (2007) <http://www.globalcmt.org/CMTsearch.html>. Accessed 2 April 2007
- Goldfinger C (1994) Active deformation of the Cascadia forearc: implications for great earthquake potential in Oregon and Washington. Dissertation thesis, Oregon State University, Corvallis, OR
- Goldfinger C, McNeill LC (2006) Sumatra and Cascadia: parallels explored. *Eos Trans Am Geophys Union* 87:52
- Goldfinger C, Mackay ME, Moore GF, Kulm LD, Yeats RS, Appelgate B (1992) Transverse structural trends along the Oregon convergent margin: implications for Cascadia earthquake potential and crustal rotations. *Geology* 20(2):141–144
- Goldfinger C, Kulm LD, Yeats RS, Hummon C, Huftile GJ, Niem AR, Fox CG, McNeill LC (1996) Oblique strike-slip faulting of the Cascadia submarine forearc: the Daisy Bank fault zone off central Oregon. In: Bebout GE, Scholl D, Kirby S, Platt JP (eds) *Subduction top to bottom*. *Geophys Monogr* 96:65–74
- Goldfinger C, Kulm LD, Yeats RS, McNeill LC, Hummon C (1997) Oblique strike-slip faulting of the central Cascadia submarine forearc. *J Geophys Res* 102:8217–8243
- Goldfinger C, Nelson CH et al (2003a) Deep-water turbidites as Holocene earthquake proxies: the Cascadia subduction zone and northern San Andreas fault systems. *Annali Geofisica* 46(5):1169–1194
- Goldfinger C, Nelson CH et al (2003b) Holocene earthquake records from the Cascadia subduction zone and northern San Andreas Fault based on precise dating of offshore turbidites. *Ann Rev Earth Planet Sci* 31:555–577
- Goldfinger C, Nelson CH, Morey-Ross A, Johnson JE, Baptista A, Zhang J, Wang K, Witter R, Priest G (2007) Interplay of structure and sediment supply may influence subduction zone rupture patches and propagation. *Eos Trans Am Geophys Union*, Fall Meet Suppl vol 88 (T52A-07)

- Goldfinger C, Grijalva K, Bürgmann R, Morey A, Johnson JE, Nelson CH, Gutiérrez-Pastor J, Ericsson A, Karabanov E, Chaytor JD, Patton J, Gràcia E (2008) Late Holocene rupture of the northern San Andreas Fault and possible stress linkage to the Cascadia subduction zone. *Bull Seismol Soc Am* 98(2):861–889
- Goldfinger C, Nelson CH, Morey A, Johnson JE, Gutierrez-Pastor J, Eriksson AT, Karabanov E, Patton J, Gracia E, Enkin R, Dallimore A, Dunhill G, Vallier T, The Shipboard Scientific Parties (2009) Turbidite event history: methods and implications for Holocene paleoseismicity of the Cascadia subduction zone. US Geological Survey Professional Paper 1661-F
- Hebenstreit GT, Murty TS (1989) Tsunami amplitudes from local earthquakes in the Pacific Northwest region of North America, part 1—the outer coast. *Mar Geodesy* 13:101–146
- Hyndman RD, Wang K (1995) The rupture zone of Cascadia great earthquakes from current deformation and the thermal regime. *J Geophys Res* 100:22133–22154
- Hyndman RD, Leonard LJ, Currie CA (2005) Test of models for the Cascadia great earthquake rupture area using coastal subsidence estimates for the 1700 earthquake. Final Report, US Geological Survey NEHRP External Grant Award 04HQGR0088
- Johnson J, Satake K, Holdahl S, Sauber J (1996) The 1964 Prince William Sound earthquake: joint inversion of tsunami and geodetic data. *J Geophys Res* 101(B1):523–532
- Kelsey HM, Nelson AR, Hemphill-Haley E, Witter RC (2005) Tsunami history of an Oregon coastal lake reveals a 4600 yr record of great earthquakes on the Cascadia subduction zone. *Geol Soc Am Bull* 117:1009–1032
- Konca AO, Avouac JP, Sladen A, Meltzner AJ, Sieh K, Peng Fang P, Li Zhenhong Z, Galetzka J, Genrich J, Chlieh C, Natawidjaja DH, Bock Y, Fielding EJ, Ji C, Helmberger DV (2008) Partial rupture of a locked patch of the Sumatra megathrust during the 2007 earthquake sequence. *Nature* 456:631–635
- Kulm LD, Von Huene R, The Shipboard Scientific Party (1973) Initial reports of the Deep Sea Drilling Project, 18. Washington, DC, US Government Printing Office, pp 97–168
- Lander JF, Lockridge PA, Kozuch MJ (1993) Tsunamis affecting the West Coast of the United States, 1806–1992. NGDC Key to Geophysical Records, Documentation no. 29
- Leonard LJ, Hyndman RD, Mazzotti S (2004) Coseismic subsidence in the 1700 great Cascadia earthquake: coastal estimates versus elastic dislocation models. *Geol Soc Am Bull* 116:655–670
- Mandal N, Chattopadhyay A, Bose S (1997) Imbricate thrust spacing: experimental and theoretical analyses. In: Sengupta S (ed) Evolution of geological structures in micro- to macro-scales, Chapter 8.1. Chapman and Hall, London
- Mann DM, Snavely PD Jr (1984) Multichannel seismic-reflection profiles collected in 1977 in the eastern Pacific Ocean off of the Washington/Oregon coast. US Geological Survey Open-File Report 84-0005
- McCaffrey R (1997) Influences of recurrence times and fault zone temperatures on the age-rate dependence of subduction zone seismicity. *J Geophys Res* 102(B10):22839–22854
- McCaffrey R, Long MD, Goldfinger C, Zwick PC, Nabelek JL, Johnson CK, Smith C (2000) Rotation and plate locking at the southern Cascadia subduction zone. *Geophys Res Lett* 27:3117–3120
- McCaffrey R, Qamar A, King RW, Wells RW, Khazaradze G, Williams C, Stevens C, Vollick JJ, Zwick PC (2007) Fault locking, block rotation and crustal deformation in the Pacific Northwest. *Geophys J Int* 169:1315–1340
- McCrorry PA, Blair JL, Oppenheimer DH, Walter SR (2004) Depth to the Juan de Fuca slab beneath the Cascadia subduction margin—a 3-D model for sorting earthquakes. US Geological Survey Data Series DS-91. <http://pubs.usgs.gov/ds/91/>. Accessed 5 Sept 2006
- McNeill LC, Piper KA, Goldfinger C, Kulm LD, Yeats RS (1997) Listric normal faulting on the Cascadia continental margin. *J Geophys Res* 102(B6):12123–12138
- McNeill LC, Goldfinger C, Kulm LD, Yeats RS (2000) Tectonics of the Neogene Cascadia forearc basin: investigations of a deformed late Miocene unconformity. *Geol Soc Am Bull* 112(8):1209–1224
- Mitchell CE, Vincent P, Weldon RJ II, Richards MA (1994) Present-day vertical deformation of the Cascadia margin, Pacific northwest, USA. *J Geophys Res* 99:12257–12277
- Mofjeld HO, Foreman MGG, Ruffman A (1997) West Coast tides during Cascadia subduction zone tsunamis. *Geophys Res Lett* 24(17):2215–2218
- Myers EP III, Baptista AM (2001) Analysis of factors influencing simulations of the 1993 Hokkaido Nansei-Oki and 1964 Alaska Tsunamis. *Nat Hazards* 23:1–28
- Myers EP III (1999) Physical and numerical analysis of long wave modeling for tsunamis and tides. Dissertation thesis, Oregon Graduate Institute of Science & Technology, Hillsboro, OR
- Nelson AR, Kelsey HM, Witter RC (2006) Great earthquakes of variable magnitude at the Cascadia subduction zone. *Quat Res* 65:354–365

- Nelson AR, Sawai Y, Jenningsc AE, Bradleya L, Gersonc L, Sherrod BL, Sabeane J, Horton BP (2008) Great-earthquake paleogeodesy and tsunamis of the past 2000 years at Alsea Bay, central Oregon coast, USA. *Quat Sci Rev* 27:747–768
- Ng MK-F, LeBlond PH, Murty TS (1990) Simulation of tsunamis from great earthquakes on the Cascadia subduction zone. *Science* 250:1248–1251
- Obermeier SF, Dickenson SE (2000) Liquefaction evidence for the strength of ground motions resulting from Late Holocene Cascadia subduction earthquakes, with emphasis on the event of 1700 AD. *Bull Seismol Soc Am* 90(4):876–896
- Okada Y (1985) Surface deformation due to shear and tensile faults in a half-space. *Bull Seismol Soc Am* 75(4):1135–1154
- Olmstead D (2003) Development in Oregon's tsunami inundation zone: information guide for developers and local government. Oregon Department of Geology Mineral Industries Open-File Report O-03-05
- Park JO, Tsuru T, Kodaira S, Cummins PR, Kaneda Y (2002) Splay fault branching along the Nankai subduction zone. *Science* 297:1157–1160
- Plafker G (1972) Alaskan earthquake of 1964 and Chilean earthquake of 1960: Implications for arc tectonics. *J Geophys Res* 77:901–925
- Preuss J, Hebenstreit GT (1998) Integrated tsunami-hazard assessment for a coastal community, Grays Harbor, Washington. US Geological Survey Professional Paper 1560 vol 2, pp 517–536
- Priest GR (1995) Explanation of mapping methods and use of the tsunami hazard maps of the Oregon coast. Oregon Department of Geology Mineral Industries Open-File Report O-95-67
- Priest GR, Allan JC (2004) Evaluation of coastal erosion hazard zones along dune and bluff backed shorelines in Lincoln County, Oregon: Cascade Head to Seal Rock, Technical Report to Lincoln County. Oregon Department of Geology Mineral Industries Open-File Report O-04-09
- Priest GR, Myers E, Baptista A, Kamphaus RA, Peterson C (1997) Cascadia subduction zone tsunamis: hazard mapping at Yaquina Bay, Oregon. Oregon Department of Geology Mineral Industries Open-File Report O-97-34
- Priest GR, Chawla A, Allan JC (2007) Tsunami hazard map of the Florence-Siuslaw River area, Lane County, Oregon. Oregon Department of Geology Mineral Industries IMS-25
- Priest GR, Goldfinger C, Wang K, Witter RC, Zhang Y, Baptista AM (2009) Tsunami hazard assessment of the Northern Oregon coast: a multi-deterministic approach tested at Cannon Beach, Clatsop County, Oregon. Oregon Department of Geology Mineral Industries Special Paper 41
- Rikitake T (1999) Probability of a great earthquake to recur in the Tokai district, Japan: reevaluation based on newly-developed paleoseismology, plate tectonics, tsunami study, micro-seismicity and geodetic measurements. *Earth Planets Space* 51(3):147–157
- Satake K, Shimazaki K, Tsuji Y, Ueda K (1996) Time and size of a giant earthquake in Cascadia inferred from Japanese tsunami records of January 1700. *Nature* 379:246–249
- Satake K, Wang K, Atwater BF (2003) Fault slip and seismic moment of the 1700 Cascadia earthquake inferred from Japanese tsunami descriptions. *J Geophys Res* 108:ESE7-1–ESE7-17
- Sawai Y, Satake K, Kamataki T, Nasu H, Shishikura M, Atwater BF, Horton BP, Kelsey HM, Nagumo T, Yamaguchi M (2004) Transient uplift after a 17th-century earthquake along the Kuril subduction zone. *Science* 306:1918–1920
- Schmidt D, Burgette R, Weldon R (2007) The distribution of interseismic locking on the central Cascadia subduction zone inferred from coastal uplift rates in Oregon. *Eos Trans Am Geophys Union* vol 88 (T52A-04)
- Seno T (2002) Tsunami earthquake as transient phenomena. *Geophys Res Lett* 29(10):1419. doi: [10.1029/2002GL014868](https://doi.org/10.1029/2002GL014868)
- Song T-RA, Simons M (2003) Large trench-parallel gravity variations predict seismogenic behavior in subduction zones. *Science* 301:630–633
- Szeliga W, Melbourne T, Santillan M, Miller M (2008) GPS constraints on 34 slow slip events within the Cascadia subduction zone, 1997–2005. *J Geophys Res* 113:B04404. doi: [10.1029/2007JB004948](https://doi.org/10.1029/2007JB004948)
- Tadepalli S, Synolakis CE (1994) The run-up of N-waves on sloping beaches. *Proc R Soc Lond A* 445:99–112
- Titov VV, Mofjeld HO, González FI, Neuman JC (1999) Offshore forecasting of Hawaiian tsunamis generated in Alaskan-Aleutian subduction zone. NOAA Technical Memorandum ERL PMEL-114
- Titov VV, González FI, Mofjeld HO, Neuman JC (2001) Project SIFT (short term inundation forecasting for tsunamis). International tsunami symposium 2001 proceedings, vol 7-2, pp 715–721
- Trehu AM, Braunmiller J, Nabelek JL (2008) Probable low-angle thrust earthquakes on the Juan de Fuca-North America plate boundary. *Geology* 36:127–130

- Tsunami Pilot Study Working Group (2006) Seaside, Oregon tsunami pilot study—modernization of FEMA flood hazard maps. National Oceanic and Atmospheric Administration OAR Special Report, NOAA/OAR/PMEL, Seattle, WA
- Walsh TJ, Caruthers CG, Heinitz AC, Myers EP III, Baptista AM, Erdakos GB, Kamphaus RA (2000) Tsunami hazard map of the southern Washington coast; modeled tsunami inundation from a Cascadia subduction zone earthquake. Wash Division of Geology and Earth Resources Geologic Map GM-49
- Wang K (2007) Elastic and viscoelastic models of crustal deformation in subduction earthquake cycles. In: Dixon T, Moore JC (eds) The seismogenic zone of subduction thrust faults. Columbia University Press, New York, pp 540–575
- Wang K, He J (1999) Mechanics of low-stress forearcs: Nankai and Cascadia. *J Geophys Res* 104(B7): 15191–15205
- Wang K, He J (2008) Effects of frictional behaviour and geometry of subduction fault on coseismic seafloor deformation. *Bull Seismol Soc Am* 98(2):571–579
- Wang K, Hu Y (2006) Accretionary prisms in subduction earthquake cycles: the theory of dynamic Coulomb wedge. *J Geophys Res* 111:B06410. doi:[10.1029/2005JB004094](https://doi.org/10.1029/2005JB004094)
- Wang K, Wells R, Mazzotti S, Hyndman RD, Sagiya T (2003) A revised dislocation model of interseismic deformation of the Cascadia subduction zone. *J Geophys Res* 108(B1):2026. doi:[10.1029/2001JB001227](https://doi.org/10.1029/2001JB001227)
- Wells RE, Blakely RJ, Sugiyama Y, Scholl DW, Dinterman PA (2003) Basin-centered asperities in great subduction zone earthquakes: a link between slip, subsidence, and subduction erosion. *J Geophys Res* 108(B10):2507. doi:[10.1029/2002JB002072](https://doi.org/10.1029/2002JB002072)
- Werner KS, Graven EP, Berkman TA, Parker MJ (1991) Direction of maximum horizontal compression in western Oregon determined by borehole breakouts. *Tectonics* 10(5):948–958
- Whitmore PM (1993) Expected tsunami amplitudes and currents along the North American coast for Cascadia subduction zone earthquakes. *Nat Hazards* 8:59–73
- Witter RC (2008) Prehistoric Cascadia tsunami inundation and runup at Cannon Beach, Oregon. Oregon Department of Geology Mineral Industries technical report to the Cannon Beach Rural Fire Protection District. Oregon Department of Geology Mineral Industries Open-File Report O-08-12
- Zhang Y, Baptista AM (2008) An efficient and robust tsunami model on unstructured grids part I: inundation benchmarks. *Pure Appl Geophys* 165(11–12):2229–2248. doi:[10.1007/s00024-008-0424-7](https://doi.org/10.1007/s00024-008-0424-7)